Determination of Cellular Strains by Combined Atomic Force Microscopy and Finite Element Modeling

Guillaume T. Charras and Mike A. Horton
The Bone and Mineral Centre, The Rayne Institute, Department of Medicine, University College London, London WC1E 6JJ, United Kingdom

ABSTRACT Many organs adapt to their mechanical environment as a result of physiological change or disease. Cells are both the detectors and effectors of this process. Though many studies have been performed in vitro to investigate the mechanisms of detection and adaptation to mechanical strains, the cellular strains remain unknown and results from different stimulation techniques cannot be compared. By combining experimental determination of cell profiles and elasticities by atomic force microscopy with finite element modeling and computational fluid dynamics, we report the cellular strain distributions exerted by common whole-cell straining techniques and from micromanipulation techniques, hence enabling their comparison. Using data from our own analyses and experiments performed by others, we examine the threshold of activation for different signal transduction processes and the strain components that they may detect. We show that modulating cell elasticity, by increasing the F-actin content of the cytoskeleton, or cellular Poisson ratio are good strategies to resist fluid shear or hydrostatic pressure. We report that stray fluid flow in some substrate-stretch systems elicits significant cellular strains. In conclusion, this technique shows promise in furthering our understanding of the interplay among mechanical forces, strain detection, gene expression, and cellular adaptation in physiology and disease.

INTRODUCTION

Many organs adapt to their mechanical environment: new bone is synthesized in response to high exercise regimen (Rubin and Lanyon, 1984), cardiac and vascular smooth muscle adapt to pump pressure (Xu, 2000), and skeletal muscle adapts to exercise levels (Russell et al., 2000). The detection and adaptation to mechanical strain are performed by the cells constituting these organs.

Many experiments in vitro have highlighted cellular detection and adaptation to mechanical stimuli using a variety of devices to apply mechanical stimulation: endothelial cells submitted to fluid flow for 24 h align with the direction of flow (Girard and Nerem, 1993), and steady and oscillating fluid shear stress can elicit calcium transients in a variety of cell types (Hung et al., 1996); cells submitted to substrate stretch realign perpendicular to the direction of strain (Hayakawa et al., 2001); chondrocytes submitted to intermittent hydrostatic pressure increase proteoglycan synthesis (Jortikka et al., 2000); osteoblasts increase their intracellular calcium concentration when subjected to micropipette poking or pulling via magnetic microbeads (Xia and Ferrier, 1992; Glogauer et al., 1995); and endothelial cells increase gene expression of endothelin-1 when subjected to microbead twisting (Chen et al., 2001). Methods of applying mechanical stimulation can be broadly divided into two categories: those that apply stimulation over the whole cell (substrate stretch, fluid shear, intermittent hydrostatic pressure), and those that stimulate only a small part of the cell body (microbead pulling, microbead twisting, micropipette poking). Results obtained with one straining system are difficult to compare to those obtained with another. Indeed, cells are most likely to detect deformations applied onto their structure or, in engineering terms, strain (deformation per unit length). Knowing the strain distributions on cell surfaces would enable results from different straining techniques to be compared to one another, and their physiological consequences to be analyzed.

Common engineering techniques such as computational fluid dynamics (CFD) or finite element modeling (FEM) can be used to compute the shear stresses resulting from fluid flow or the strain distributions due to mechanical stimulation. CFD enables velocity and pressure distributions generated by a fluid flowing over a surface to be determined and, therefore, shear stress distribution can be determined. CFD has been utilized with success to investigate the flow of blood through arteries and their bifurcations (Long et al., 2001). Barbee et al. (1995) calculated the shear stresses due to fluid flow over an endothelial cell monolayer whose topography had been acquired using atomic force microscopy (AFM). Used in conjunction with FEM, this can yield the cellular strains elicited by fluid shear stress. Indeed, FEM allows the strain distribution due to a given set of loading and boundary conditions applied onto a structure whose material properties are known to be determined. FEM has been applied with success to modeling and determining the strain distributions within whole organs such as bone (van Rietbergen et al., 1999), cartilage (Gu et al., 1997), or the arterial wall (for a review see Simon et al. (1993)), but has seldom been applied to individual cells due to lack of precise data on cellular material properties or shape. Riemer-McReady and Hollister (1997) modeled an osteocyte embedded within its lacuna to find the strains

Submitted January 14, 2002, and accepted for publication March 4, 2002.
Address reprint requests to Dr. Mike Horton, 5 University Street, London WC1E 6JJ, UK. Tel.: 44-207-679-6169; Fax: 44-207-679-6219; E-mail: m.horton@ucl.ac.uk.

0006-3495/02/08/858/22 $2.00

applied to the cell by a uniform compression of the matrix in which it was embedded. Guilak and Mow (2000) and Wu and Herzog (2000) modeled a chondrocyte embedded within a cartilaginous matrix. In all three cases the cells were modeled as spheres with homogenous properties, hence ignoring potential inhomogeneities in material properties or topology. Other finite element models have concentrated on predicting cellular material properties from the cytoskeletal structure (Hansen et al., 1996), predicting the rearrangement of the cytoskeleton (Picart et al., 2000), or the evolution of the cell shape in response to micropipette aspiration (Drury and Dembo, 1999). Although many methods exist to measure the bulk cellular material properties, only AFM enables the three-dimensional profile of cell surfaces to be acquired at high resolution together with their material property distribution (for a review see Radmacher (1997)).

In this study we combined AFM with FEM and CFD to calculate the strain distributions resulting from common whole-cell mechanical stimulation techniques. Experimentally acquired cell profiles and material property maps acquired by AFM were converted into three-dimensional finite element models. Different sets of boundary and loading conditions were applied to the cell models to simulate straining experiments (substrate stretch, fluid shear, and intermittent hydrostatic pressure). Common micromanipulation experiments (microbead pulling and twisting, micropipette poking) were modeled on a small subcellular volume and strain distributions were calculated to provide a comparison to the whole-cell straining experiments. Cellular adaptation to mechanical stresses was simulated by increasing the elastic modulus of the cells and examining its effect on the strain distributions. The different parameters pertaining to the stimulation method were varied and their effect on the strain distributions was examined. In addition, we used these models to calculate the strain magnitudes resulting from experiments by other groups and compared the strain levels needed to trigger the reported detection mechanisms and downstream cellular responses.

In conclusion, we report for the first time the application of AFM in conjunction with FEM and CFD to calculate the strain distributions in cells resulting from common methods of mechanical stimulation. The knowledge of these strain distributions will enable different straining experiments to be compared to each other. Moreover, these data should aid our understanding of whether strains induced by commonly used straining techniques are detected via different intracellular signaling pathways.

MATERIALS AND METHODS

Experimental data

Cell culture

Osteoblasts were isolated from the long bones of neonatal rats by mechanical disaggregation and cultured for 72 h at 37°C in an atmosphere of 5% CO_2 in air in DMEM (Gibco Life Technologies, Paisley, UK) supplemented with 10% FCS, 2% glutamine, 2% penicillin streptomycin, 2% 1 M HEPES, pH 7.0.

Immunostaining and confocal microscopy

Immunostaining was performed as described in Nesbitt and Horton (1997). Briefly, the cells were fixed in a PBS solution containing 2% formaldehyde and 0.1% glutaraldehyde, and permeabilized in ice-cold Triton X-100 buffer for 5 min at 4°C. They were then incubated with monoclonal anti-paxillin (Transduction Laboratories, Lexington, KY), a focal contact protein, for 30 min, FITC-labeled goat anti-mouse Ig antibody (Dako, Denmark) for 30 min, and rhodamine-phalloidin (Molecular Probes Europe, Leiden, The Netherlands) for 30 min. All coverslips were imaged with a 100× oil-immersion objective on a Leica confocal microscope running TCS NT (Leica, Bensheim, Germany). Fluorescent images were sequentially collected in 0.4-μm steps with emission wavelengths of 488 and 568 nm for the FITC and TRITC fluorophores, respectively. The images were then post-processed using Imaris software (Bitplane Ag, Zürich, Switzerland) on an SGI O_2 workstation (SGI, Mountain View, CA).

Atomic force microscopy

A Thermomicroscopes Explorer (Thermomicroscopes, Sunnyvale, CA) interfaced onto an inverted microscope (Nikon Diaphot 300, Nikon UK, Kingston, UK) was used to acquire the material properties of the cells (Lehenkari et al., 2000). The measurements were carried out using soft V-shaped cantilevers with pyramidal tips ($k = 0.032$ N·m^{-1}, model 1520, Thermomicroscopes) and these were calibrated in air before experimentation.

Osteoblastic cells cultured on glass coverslips were transferred to the AFM sample holder and examined in physiological buffer (127 mM NaCl, 5 mM KCl, 2 mM $MgCl_2$, 0.5 mM $Na_2H\ PO_4$, 2 mM $CaCl_2$, 5 mM $NaHCO_3$, 10 mM glucose, 10 mM HEPES, 0.1% BSA adjusted to pH 7.4). For each cell, force-distances curves were collected at points on a 50 × 50 or 100 × 100 grid. The approach speed used for the force-distance curves was 5 μm·s^{-1} to minimize contributions of cellular viscoelasticity to the estimated cellular elasticity (A-Hassan et al., 1998).

Material property measurement

Cellular material properties were evaluated as described in Radmacher (1997). Briefly, the cell was assumed to be a homogenous half space and the tip conical. The force F needed to produce an indention of depth δ in a half-plane with an elastic modulus E is (Johnson, 1985):

$$F_{\text{conical}} = \frac{2}{\pi}\frac{E}{(1-\nu^2)\tan(\alpha)}\delta^2 \qquad (1)$$

With α the opening angle of the conical tip and ν the local Poisson ratio. Knowing the cantilever stiffness and by fitting the theoretical curve to the experimental data, the elastic modulus can be deduced (Radmacher, 1997). The cellular Poisson ratio was assumed to be 0.3, in line with experimental measurements in live cells (0.25 ± 0.05, Maniotis et al., 1997). It is necessary to choose a value of the Poisson ratio, as experimentally acquired force-distance curves fitted with Eq. 1 cannot yield both the cellular elasticity and Poisson ratio. A custom-written program running under Pv-Wave (Visual Numerics, Boulder, CO) on an SGI O_2 workstation was used to fit the force-distance curves automatically.

The spatial resolution of the material property maps could be estimated by calculating the diameter of the tip-cell contact area. Using Eq. 1, one can find δ and, assuming that the indentation is cone-shaped, the diameter of contact is $d = 2\delta\tan(\alpha)$. For $\alpha = 30°$, $E = 1$ kPa, $F = 1$ nN, $\nu = 0.3$, we find $d = 1.04$ μm. Hence, 100 × 100 grids, which sample material

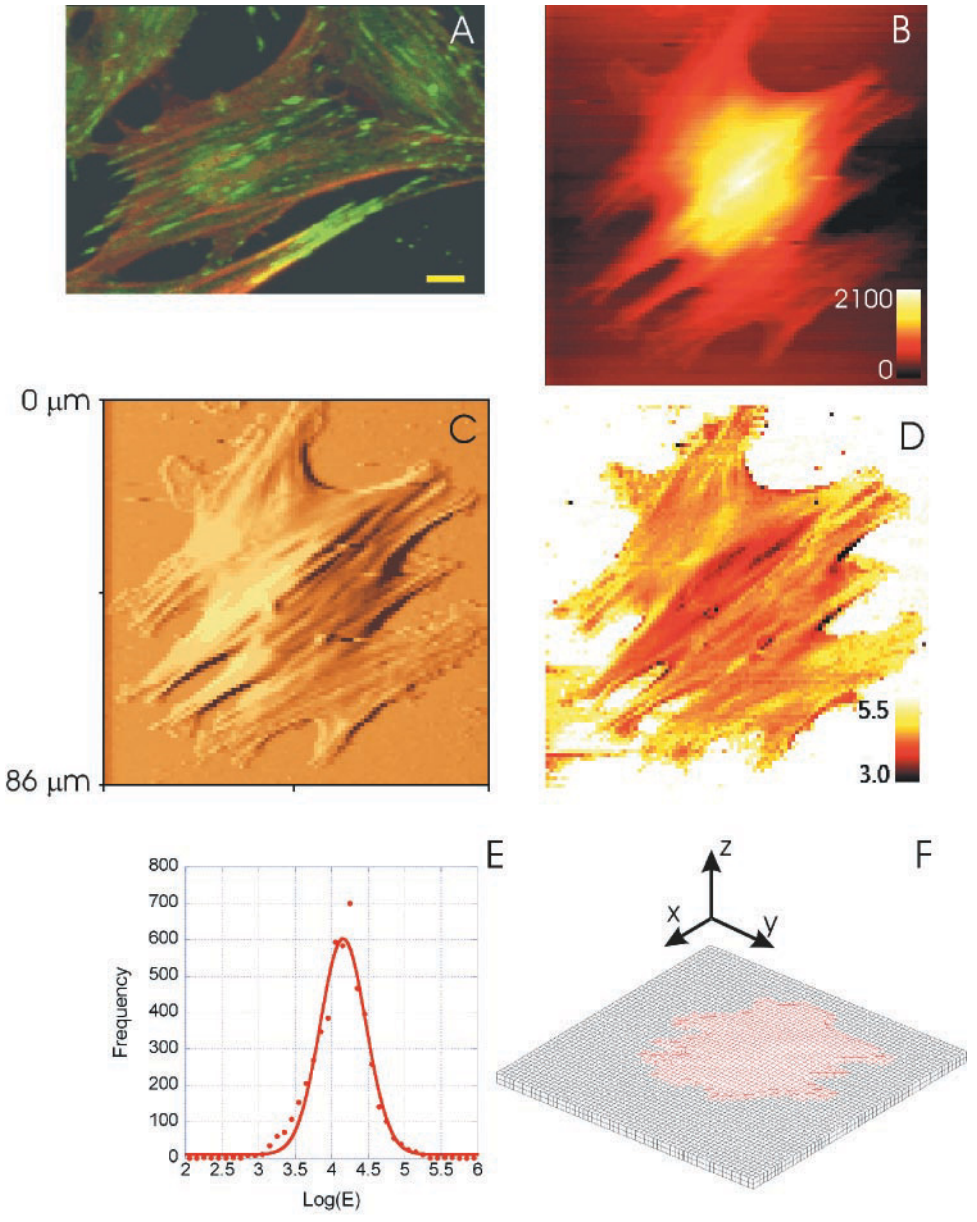

FIGURE 1 Characterization and primary data acquisition from osteoblasts. (*A*) A typical osteoblast stained for F-actin (*red*) and focal contact protein paxillin (*green*). Bar = 10 μm. (*B*) Height map of a primary osteoblast collected on a 100 × 100 grid. The cell reached a maximum height of 2.1 μm. (*C*) A pseudo three-dimensional image of the same cell. (*D*) The decimal logarithm of the material property distribution of the cell. The material properties varied between 1 and 100 kPa (or 3–5 in log(Pa), *D* and *E*). (*E*) The cumulated material property distribution of 10 osteoblasts. A Gaussian curve was fitted to the experimental distribution. (*F*) The same cell (*red*) converted into a three-dimensional finite element model and plated onto a perfectly flat substrate (*black*).

properties every micrometer, are the highest resolution that can be attained without excessive spatial overlap in measurements.

Numerical modeling for whole-cell mechanical models

The AFM scans of 10 osteoblasts were converted into three-dimensional finite element models incorporating the experimentally measured elasticities and topographies using a custom-written program running under PvWave.

Generation of whole-cell models

The cells were "virtually" extracted from their experimental substrate and plated onto a flat substrate with a Young's modulus of 4 GPa. The models (Fig. 1 *F*) had 50 × 50 elements in the *x*- and *y*-directions, a resolution of 2 μm, and ~7000 elements. The resolution in the *z*-direction was chosen to be the same as in the *x*- and *y*-directions. An additional zone 20 μm wide was added around the model to reduce boundary effects. The substrate was two elements thick. The number of elements at a given location in the cell was equal to its height divided by the *z*-resolution rounded up to the next integer. Most cells had between one and two elements in their height. Cell

and substrate were presumed to be uniformly bound along their contact area rather than in a discrete number of points representing the cellular focal adhesion complexes (Fig. 1 *A*). The cells and the substrate were modeled with eight-noded parametric volumic elements. Because of the large number of different elastic moduli within a cell, the cellular distributions were grouped into 10 material property collectors with the following elasticities:

$$E_i = \frac{E_{max} - E_{min}}{10} \cdot \left(i + \frac{1}{2}\right), \quad i = 0, \ldots, 9 \qquad (2)$$

With E_{max} and E_{min} the maximum and minimum elasticities of the cell modeled.

Physical model

As we were interested only in the static solutions for whole-cell strains, all materials were assumed to be linear elastic and isotropic (Zhu et al., 2000). Cell and substrate had a Poisson ratio of 0.3 (Maniotis et al., 1997). Appropriate boundary conditions and forces were applied to the models to simulate substrate stretch or intermittent hydrostatic pressure.

The linear elastic continuum mechanics equations (Timoshenko and Goodier, 1970) were then solved to find the strain distributions exerted on the cells. In its simplest expression, engineering strain ϵ can be defined as the length variation dl per unit length l ($\epsilon = dl/l$). Engineering strain is usually expressed in percent variation of length or microstrain ($\mu\epsilon$) with 1% strain = 0.01 ϵ = 10,000 $\mu\epsilon$. All of the finite element calculations were carried out with CAST3M, a general-purpose finite element solver with an integrated pre- and post-processor (CAST3M, Commissariat à l'Energie Atomique, Saclay, France, kk2000@semt1.smts.cea.fr., available free for universities) and were run either on an SGI O_2 or a standard PC.

Boundary conditions

Substrate stretch. For the substrate stretch simulations, a displacement equivalent to 0.1% stretch in the *x*-direction was applied to one end of the substrate and the other side was constrained in the *x*-direction. The sides running parallel to the *x*-direction were constrained in the *y*-direction. The underside of the substrate was constrained in the *z*-direction (All boundary conditions are represented in Fig. 2 *A*).

To assess the effect of the cellular Poisson ratio on the strain magnitude, ν was varied, for the whole mesh, between 0.2 and 0.5 while applying a stretch of 0.1% along the *x* axis. To assess the effect of stretch direction, the simulated direction of stretch was varied and had angles of 0°, 30°, 45°, 60°, and 90° with the *x* axis, while keeping stretch magnitude and Poisson ratio constant. These analyses were carried out on one osteoblast model only, as the strain distributions for the other cells would vary similarly due to the linear elastic nature of the mechanical model.

Intermittent hydrostatic pressure. For the intermittent hydrostatic pressure experiments, the underside of the substrate was fully constrained and a hydrostatic pressure of 5 Pa was applied to the top surface (All boundary conditions are represented in Fig. 3 *A*). To assess the effect of the Poisson ratio on cellular strain distributions, it was varied, for the whole mesh, between 0.2 and 0.5 while keeping the pressure constant. This analysis was carried out on one cell model only.

Generation of osteocyte models

The material properties of osteocytes were assumed to be the same as those of osteoblasts. As osteocytes and their cavities are ellipsoidal (Marotti et al., 1992), we modeled only half of the cell-cavity complex, thereby assuming that the other half of the cell was perfectly identical. To simulate that osteocytes were embedded in the bone matrix, the cell models were covered by a layer of matrix elements forming a brick with a "mold" of the cell on the underside. The cell and the matrix were assumed to be uniformly bound along their surface of contact. The underside of this model was constrained in the *z*-direction. A displacement equivalent to 0.1% compression in the *x*-direction was applied to one end of the block of matrix and the other side was constrained in the *x*-direction. The sides running parallel to the *x*-direction were constrained in the *y*-direction. The bone matrix was assumed to have an elasticity of 4 GPa, in agreement with experimentally measured values (Mente and Lewis, 1989).

Numerical modeling for fluid shear simulations

To examine the strain distributions resulting from fluid flow on cells, the calculations had to be performed in two distinct steps. First, a CFD model had to be generated to calculate the flow lines and shear stresses resulting from flow over the cellular profile. Second, an FE model of the cell was generated and the shear stresses from the CFD simulation were applied to the mechanical model. The strain distribution resulting from these could be calculated. As the cellular deformations were small (<0.1%), we assumed that the cellular deformations did not significantly affect the flow lines around the cell profile, and hence we did not need to iterate the process.

Generation of the models

For the fluid flow simulations, the material property distributions and topographies were reduced to a 25 × 25 grid to reduce calculation time and were converted into a three-dimensional finite element model. An entrance and an exit, 10 μm wide, were added to reduce transitory effects.

First, a CFD model of the cell and substrate surface was created with eight-noded linear volumic fluid flow elements (Fig. 4 *A*). The CFD model had a height of 16 μm, which was over fourfold greater than the average height perturbation introduced by the cell profile.

As a second step, an FEM model of the cell was created with the material properties and the topographies obtained from experimental measurements (Fig. 4 *B*). The substrate was two elements thick and the cellular material was one element thick.

Computational fluid dynamics: physical model and boundary conditions

The cell surface was subjected to a laminar flow of an incompressible viscous fluid with a parabolic profile (Fig. 4 *A*). We assumed that the flow on the top surface of the model was not significantly perturbed by the cell profile and therefore imposed a constant velocity u_{max}. We assumed that the cell did not significantly perturb the flow in the transverse horizontal direction and imposed a condition of no transverse flow on the side surfaces. The velocity on the cell-substrate surface was imposed to be 0 (all boundary conditions are represented in Fig. 4 *A*). The CFD code (CAST3M) solved the Navier-Stokes equations (Currie, 1993) using a finite-element approach and output the velocities and pressures for each element of the CFD model:

$$\rho \frac{D\mathbf{v}}{Dt} = -\nabla p + \mu \nabla^2 \mathbf{v} \qquad (3)$$

$$\nabla \cdot \mathbf{v} = 0 \qquad (4)$$

The shear stresses tensor and shear stresses were then calculated as follows (Currie, 1993):

$$\tau_{ij} = -p\delta_{ij} + \mu\left(\frac{\partial v_i}{\partial x_j} + \frac{\partial v_j}{\partial x_i}\right) \qquad (5)$$

$$\boldsymbol{\tau}_i = \sum_{j=x,y,z} \tau_{ij} \cdot \mathbf{e}_i = \tilde{\tau} \cdot \mathbf{e}_i \qquad (6)$$

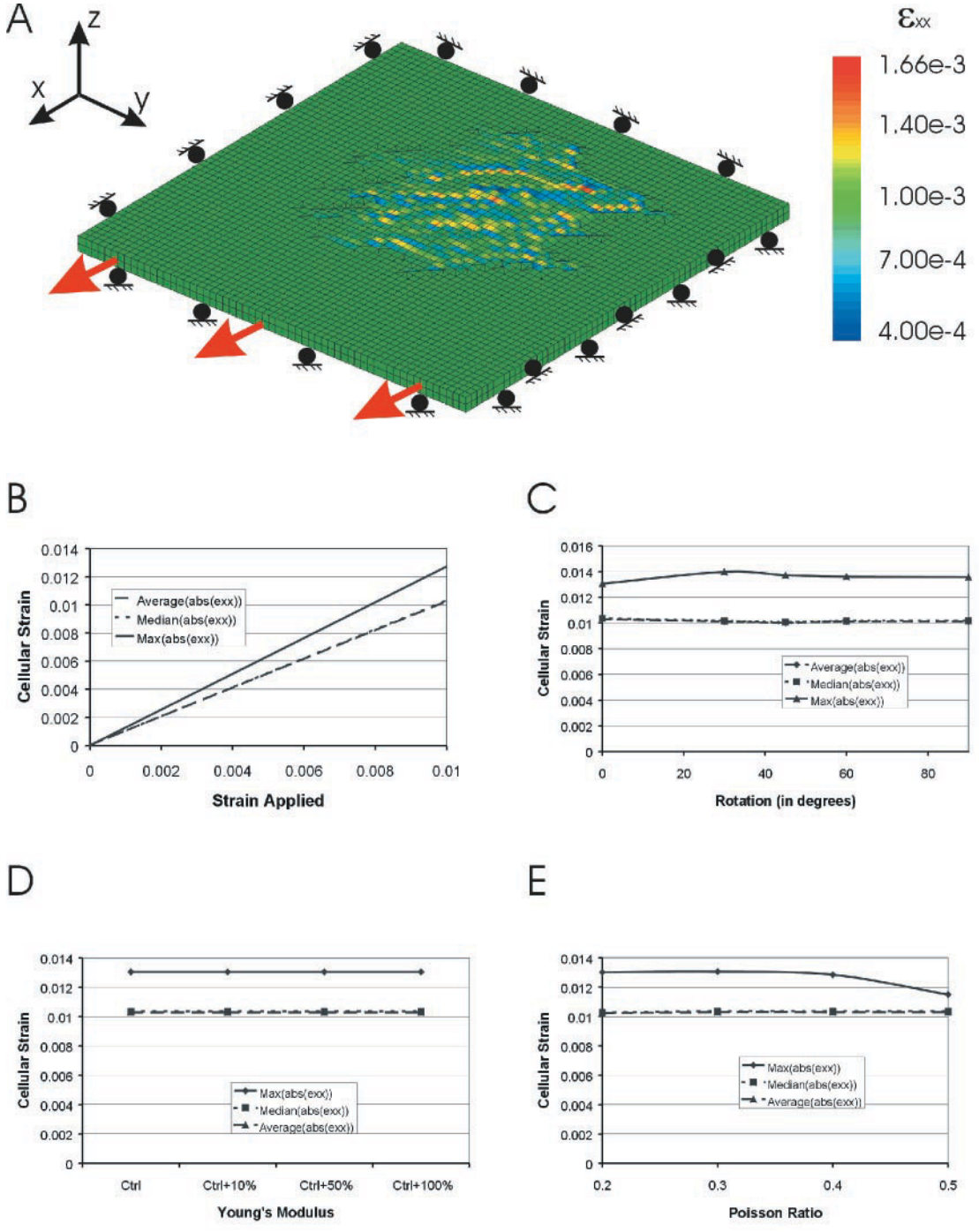

FIGURE 2 The effect of substrate stretch. (*A*) The distribution of ϵ_{xx} on the cell and substrate surface for a 0.1% stretch. The red arrows indicate the directions of stretch and the balls indicate a sliding boundary condition. One grid division is 2 μm in length. (*B*) Evolution of the maximum, median, and average cellular strains for commonly used substrate stretches. These evolutions are averaged over 10 cells. (*C*) The effect of the direction of stretch on the cellular strains (ϵ_{11}) in one cell. The direction is expressed by its angle with the *x* axis. (*D*) The effect of increasing elasticities on cellular strains (ϵ_{xx}) for a fixed stretch of 0.1% in one cell. (*E*) The evolution of cellular strains (ϵ_{xx}) with cellular Poisson ratio for a stretch of 0.1% in one cell.

With δ_{ij} the Kronecker delta, ρ the density of the fluid, v_i the velocity of the fluid flow in the *i* direction, τ_{ij} the element of the shear tensor τ in position *ij*, $\boldsymbol{\tau}_i$ the resulting shear stress vector in the *i* direction, $\mathbf{e}_i$ the directing vector *i* of the orthonormal base of vectors, and μ the cinematic viscosity of the fluid; ρ and μ were assumed to be the same as for water (respectively 1000 kg·m^{-3} and 10^{-3} N·s·m^{-2}); u_{max} was adjusted to give rise to a shear stress of 5 Pa (50 dyn·cm^{-2}) on a flat substrate and was 0.046 m·s^{-1}.

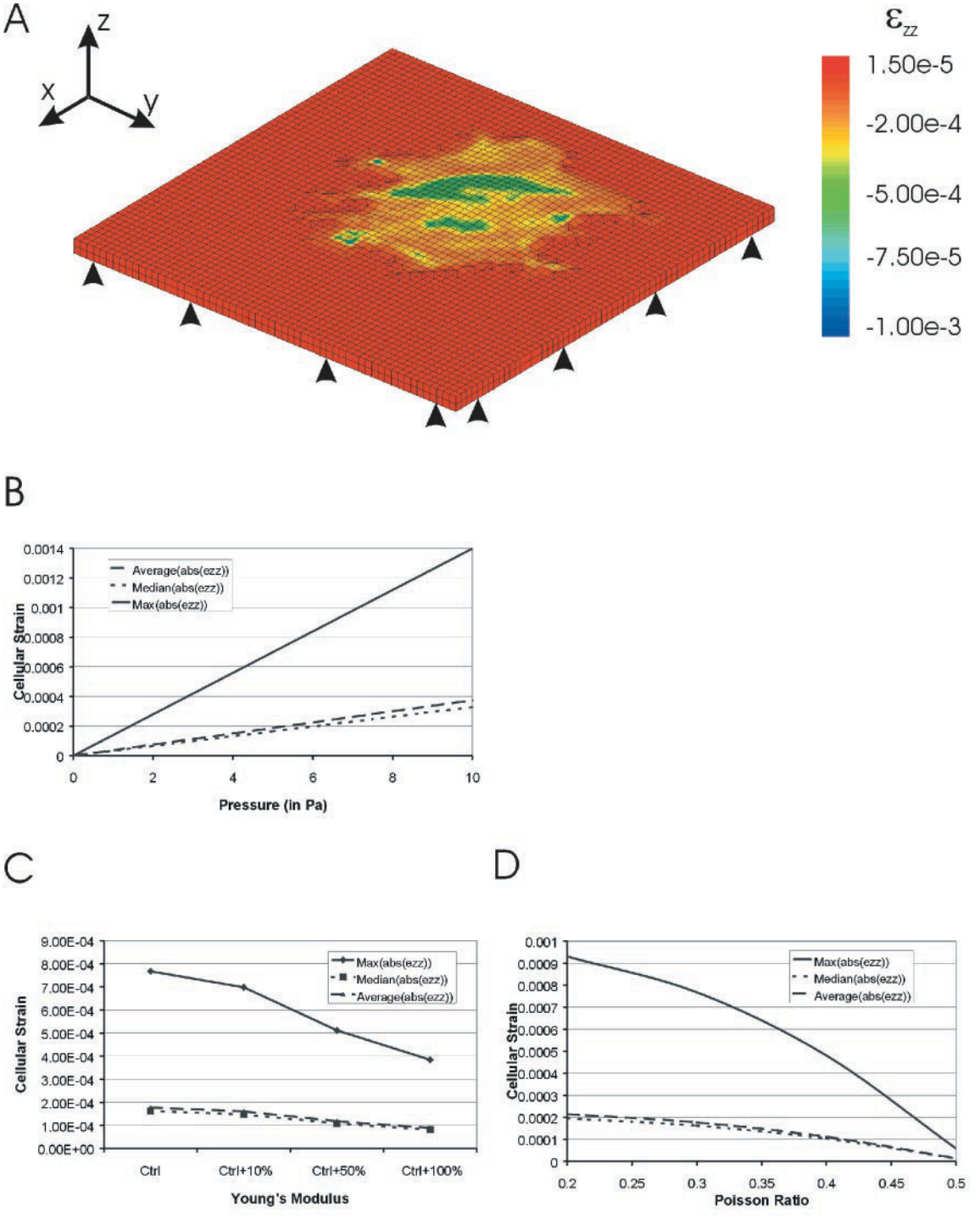

FIGURE 3 The effect of hydrostatic pressure. (*A*) The distribution of ϵ_{zz} on the cell and substrate for a 5 Pa hydrostatic pressure. Black triangles indicate where the substrate was fully constrained. Cellular strains are maximal in the nuclear area. One grid division is 2 μm in length. (*B*) The evolution of maximum, average, and median vertical strains as a function of pressure. These evolutions are averaged over 10 cells. (*C*) The evolution of cellular strains (ϵ_{zz}) with increasing Young's modulus for a pressure of 5 Pa in one cell. (*D*) The effect of the Poisson ratio on cellular strains (ϵ_{zz}) for a pressure of 5 Pa in one cell.

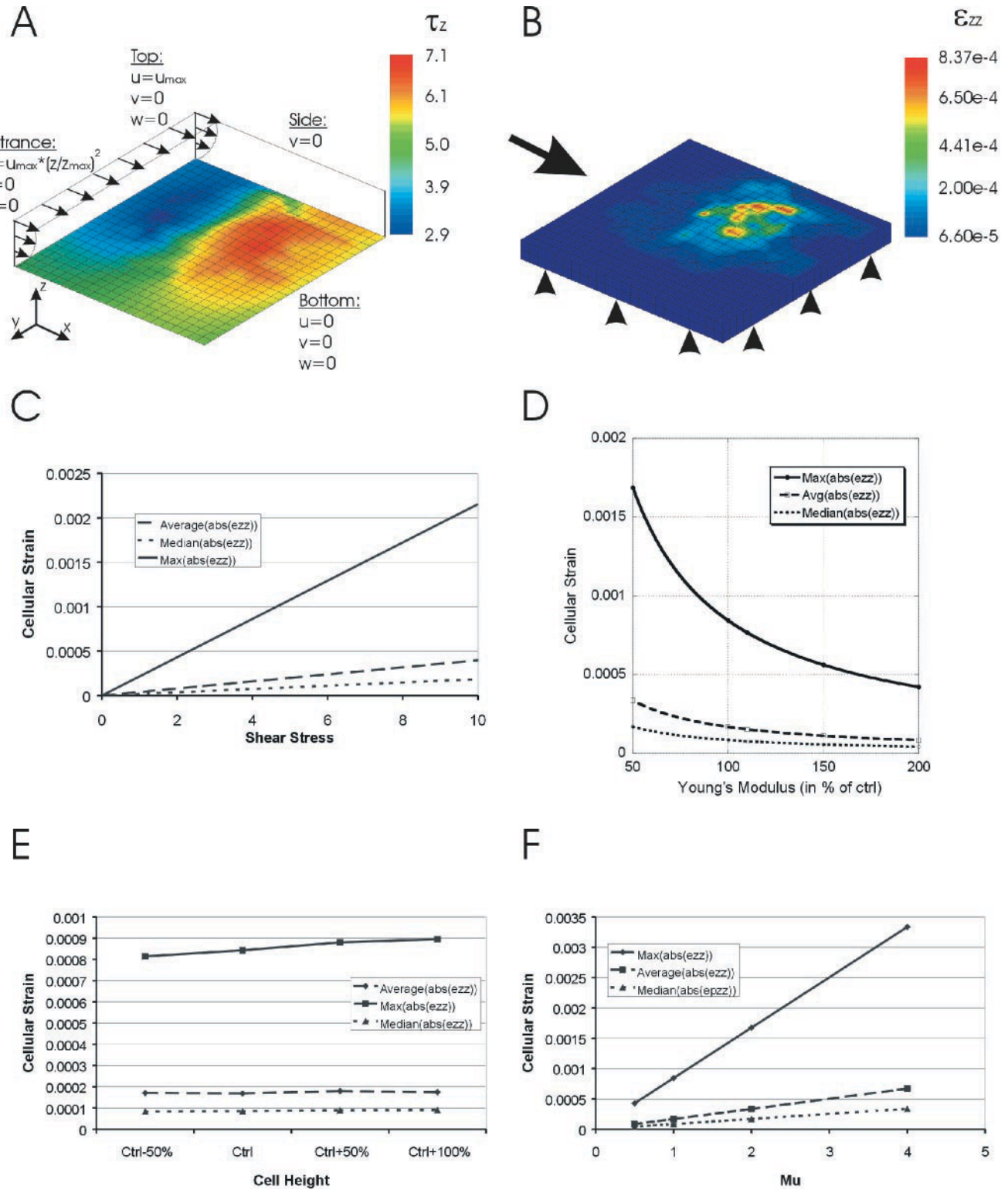

FIGURE 4 The effect of fluid shear. (*A*) The shear stress resultant in the *z*-direction (τ_z) for a nominal 5 Pa shear stress on a flat substrate. The shear stresses are tensile and lower upstream and higher downstream. The imposed parabolic flow profile is shown at the entry and the boundary conditions are indicated on the graph. (*B*) The vertical strain distribution (ϵ_{zz}) for a cell submitted to fluid shear stresses. Black triangles indicate where the substrate was fully constrained. The cellular strains are maximal downstream from the cell apex and in the cellular region. In *A* and *B*, the arrow indicates the direction of flow. (*C*) The maximal, average, and median vertical cellular strains elicited by commonly used values of shear stress averaged over 10 cells. (*D*) The evolution of cellular strain (ϵ_{zz}) with Young's modulus for a shear stress of 5 Pa in one cell. The experimental data were fitted with a power-law ($r^2 > 0.99$). (*E*) The effect of cell height on cellular strains (ϵ_{zz}) for a shear stress of 5 Pa in one cell. (*F*) The evolution of cellular strain (ϵ_{zz})with the cinematic viscosity μ for a fixed flow velocity in one cell.

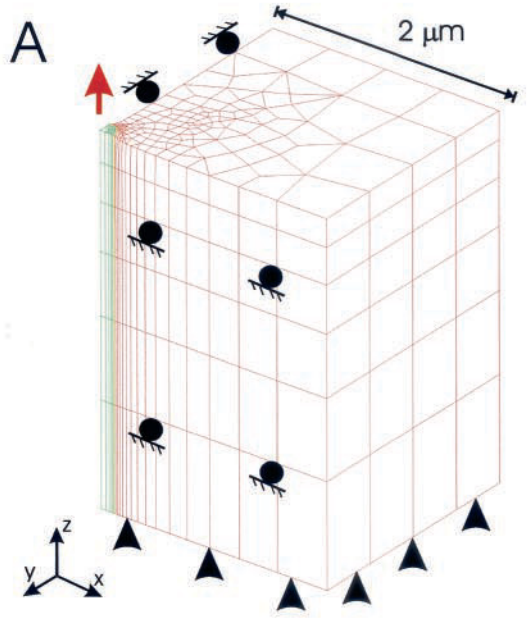
A
2 μm
z
y
x

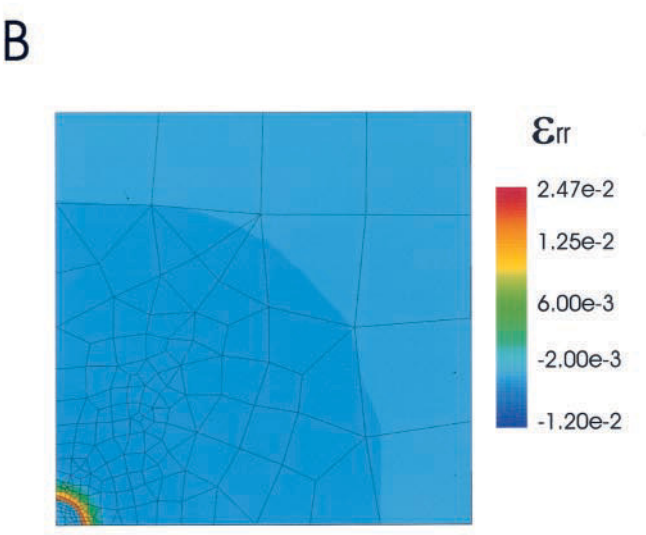
B
Err
2.47e-2
1.25e-2
6.00e-3
-2.00e-3
-1.20e-2

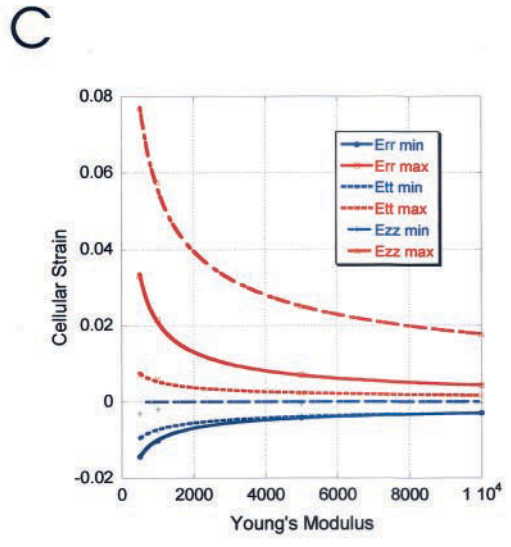
C
Cellular Strain
Young's Modulus
Err min
Err max
Ett min
Ett max
Ezz min
Ezz max

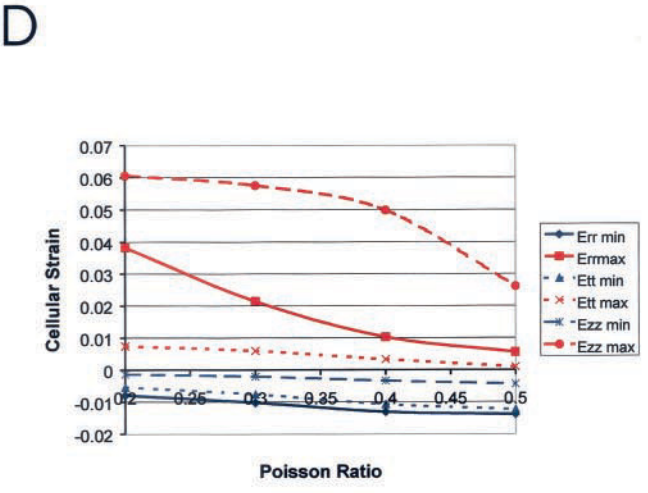
D
Cellular Strain
Poisson Ratio
Err min
Errmax
Ett min
Ett max
Ezz min
Ezz max

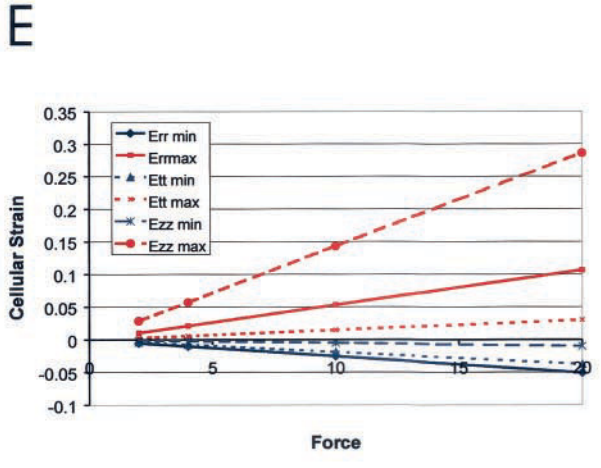
E
Cellular Strain
Force
Err min
Errmax
Ett min
Ett max
Ezz min
Ezz max

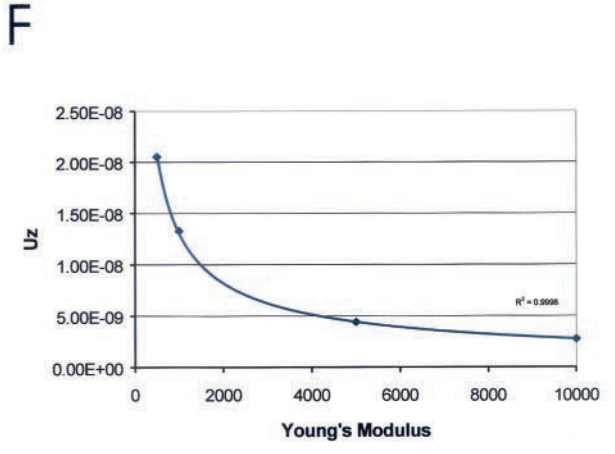
F
Uz
Young's Modulus

Finite element modeling: physical model and boundary conditions

All materials were assumed to be linear elastic and isotropic. The Poisson ratio was assumed to be 0.3. The model was fully constrained on the bottom surface and the shear stresses derived from the CFD calculation were multiplied by the surface normals and imposed onto the surface nodes (Fig. 4 *B*).

Variation of the physical parameters

To assess the effect of the cinematic viscosity μ on the cellular strains, its value was varied between 5×10^{-4} and 4×10^{-3} N·s·m^{-2} while keeping all other parameters constant. The effect of cell height on cellular strain was assessed by varying it between 50 and 200% of the original height, all other parameters being constant. Finally, the influence of the cellular Poisson ratio was evaluated by varying it, for the whole mesh, between 0.2 and 0.5 while keeping the other variables constant. These analyses were only performed for one cell model, as the other cell models would show identical trends.

Numerical modeling for micromanipulation models

Micromanipulation techniques apply mechanical stimuli only to small areas of the cell inducing large local strains. Therefore, finer meshes are needed to calculate the strain distributions with reasonable accuracy. Modeling the whole cell with a suitable mesh refinement would be unpractical, as the memory space and calculation time needed become inordinate.

Based on our experience in modeling cellular indentation by a spherical AFM tip (Charras et al., 2001), we decided to model only a small volume of the cell and assume that the material was isotropic and linear elastic. The Young's modulus was chosen to be 1 kPa, the lower value for cellular material properties, hence giving an upper bound of the cellular strains. The Poisson ratio was chosen to be 0.3 (Maniotis et al., 1997).

Magnetic microbead pulling

In magnetic microbead pulling experiments, ferromagnetic beads coated with collagen are sprinkled over a cell layer and left to settle for 30 min. The collagen-coated beads bind to the cells via integrin cell adhesion receptors and the cells are washed several times to remove unbound beads. During the experiment a magnetic field is applied to the cells and the microbeads are displaced vertically, pulling the cell with a force of 4 pN over the area of contact (Glogauer and Ferrier, 1998).

To determine the area of contact of the magnetic microbeads with the cell surface, we assumed that when the microbeads contact the cells they indent the cellular material with a force F_w equal to their weight minus the buoyancy force, thus creating an indentation of radius a (Johnson, 1985).

$$F_w = (\rho_{Fe_3O_4} - \rho_{H_2O}) \cdot \frac{4}{3} \pi R^3 \cdot g \tag{7}$$

$$a = \left(\frac{3}{4} \frac{F_w R (1 - \nu^2)}{E} \right)^{1/3} \tag{8}$$

With R the bead radius, ν the Poisson ratio, E the elastic modulus, g the universal gravitational constant (9.81 kg·m·s^{-2}), ρ_{Fe3O4} the volumic mass of magnetite (4897 kg·m^{-3}), and ρ_{H2O} the volumic mass of water (10^3 kg·m^{-3}). The radius of the beads was chosen to be 2 μm (Glogauer and Ferrier, 1998) yielding a radius of contact of 0.12 μm.

Taking the symmetries of the problem into account, only one-quarter of the space was modeled (Fig. 5 *A*). A box 2 μm long in the x- and y-directions and 3 μm thick was meshed with 20-noded parametric volumic elements with a higher density in the area of contact (shown in green in Fig. 5 *A*), and particularly at the boundary between the tethered and untethered region. The model was constrained in displacement in the z-direction at its base and in the x- and y-directions, respectively, on the y- and x-sides in which the pulling was applied (Fig. 5 *A*). The other sides were left free. To simulate magnetic pulling, a uniform force was applied to the top surface nodes in the area of contact. The area of contact was constrained in the x- and y-directions to simulate integrin linkages between the cell surface and the bead. The experimentally controllable parameters are the force applied (through the magnetic field), and the radius of the microbeads.

The importance of the Poisson ratio was investigated by varying it, for the whole mesh, between 0.2 and 0.5, recalculating the radius of indentation accordingly and solving for the strain distribution with the new Poisson ratio with $E = 1$ kPa and $F = 4$ pN. The total force applied to the bead was varied between 2 and 20 pN, and the cellular strains resulting were calculated with $E = 1$ kPa and $\nu = 0.3$.

Microbead twisting

During microbead twisting experiments the ferromagnetic beads are tethered to the cells following a similar protocol as for microbead pulling, but are coated with RGD, an integrin receptor agonist (Wang and Ingber, 1994). The beads are then magnetized using a large magnetic pulse and a much smaller magnetic field is used to make them rotate and apply a torque onto the cell cytoskeleton via integrin receptors (Wang and Ingber, 1994).

The area of contact of the beads with the cell surface was calculated as for magnetic bead pulling. The problem only has one plane of symmetry and accordingly, we modeled one half-space (Fig. 6 *A*). A 4 μm $\times$ 2 μm box in the x- and y-directions and 3 μm thick was meshed with 20-noded parametric volumic elements with a higher density in the area of contact (shown in green in Fig. 6 *A*) and particularly at the boundary between the region in contact and the free region. The model was constrained in displacement in the z-direction at its base, in the y-direction on the plane of symmetry, and in the x- and y-directions, respectively, on the y- and x-sides on the other vertical surfaces (Fig. 6 *A*). To simulate the magnetic twisting, the nodes on the surface of contact were rotated by an angle α around the y axis of the contact disk. The force and pressure applied could be calculated by extracting the resultant of this imposed displacement. The area of contact was constrained in the x- and y-directions to simulate integrin linkages between the cell surface and the bead. The read-out variable for these experiments is the angle of rotation and the control is effected via the pressure applied. Wang and Ingber (1994) report a maximal pressure of 4 Pa applied on the area of contact.

The importance of the Poisson ratio was investigated by varying it, for the whole mesh, between 0.2 and 0.5, recalculating the radius of indenta-

FIGURE 5 The effect of microbead pulling. (*A*) The cellular deformation amplified fourfold resulting from microbead pulling for a 4 pN force. The microbead is tethered on the top surface in the region in green. The red arrow indicates the direction of bead movement. Black triangles indicate where the substrate was fully constrained. The balls indicate a sliding boundary condition. (*B*) The radial strain distribution (ϵ_{rr}) on the top surface resulting from microbead pulling. High tensile strains are present on the borders of the tethered region. (*C*) The evolution of cellular strains as a function of cellular elasticity for a force of 4 pN. The results were fit with a power-law ($r^2 > 0.95$ except "ϵ_{rr} min"). (*D*) The evolution of cellular strains with the Poisson ratio for a force of 4 pN. (*E*) The evolution of cellular strains with increasing force (in pN). (*F*) The vertical displacement as a function of the cellular Young's modulus for a force of 4 pN. The experimental results were fit with a power-law ($r^2 > 0.99$).

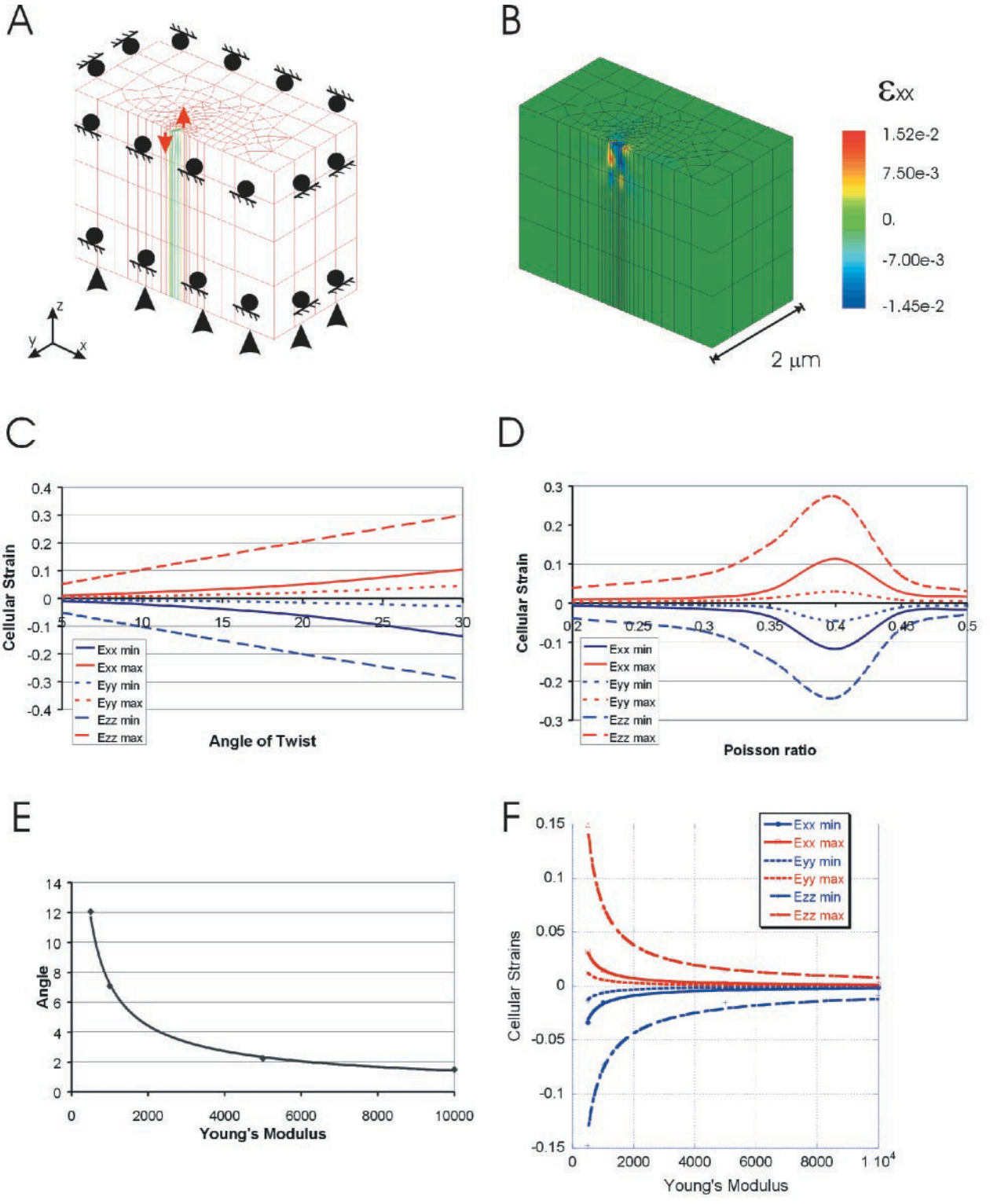

FIGURE 6 The effect of microbead twisting. (*A*) The cellular deformation amplified twofold resulting from microbead twisting for a 4 Pa pressure. The microbead is tethered on the top surface in the region in green. The red arrows indicate the movement of the borders of the tethered region. Black triangles indicate where the substrate was fully constrained. The balls indicate a sliding boundary condition. (*B*) The strain distributions (ϵ_{xx}) resulting from microbead twisting. High tensile strains are present on either side of the tethered region. (*C*) The evolution of cellular strains with the angle of twist. (*D*) The evolution of cellular strains with the Poisson ratio for a pressure of 4 Pa. (*E*) The angle of twist as a function of the cellular Young's modulus for a pressure of 4 Pa. The experimental results were fit with a power-law ($r^2 > 0.99$). (*F*) The evolution of cellular strains as a function of cellular elasticity. The results were fit with a power-law ($r^2 > 0.95$).

tion accordingly and solving for the strain distribution with the new Poisson ratio with $E = 1$ kPa and $p = 4$ Pa. The rotation applied to the bead was varied between 5° and 40°, and the resulting cellular strains were calculated with $E = 1$ kPa and $\nu = 0.3$. The effect of the radius of contact was assessed by varying it between 0.1 and 0.6 μm with $p = 4$ Pa, $E = 1$ kPa, and $\nu = 0.3$.

Micropipette poking

Micropipette poking consists of lightly indenting the cell surface with a blunt micropipette. We assumed that this was similar to indenting the cell surface with a rigid spherical indentor with a radius of 1.5–3 μm.

This experiment was modeled similarly to cellular indentation by a glass sphere using AFM (Charras et al., 2001). Taking the symmetries of the problem into account, only one-quarter of the space was modeled. A box 15 μm in length in the *x*- and *y*-directions and 4 μm thick was meshed with 20-noded parametric volumic elements, with a higher density of elements in the area of indentation and particularly at the boundary between the indented (shown in green in Fig. 7 *A*) and the free regions. The model was constrained in displacement in the *z*-direction at its base and in the *x*- and *y*-directions, respectively, on the *y*- and *x*-sides in which the indentation was performed (Fig. 7 *A*). The other sides were left free. The cellular material was assumed to be linear elastic and isotropic. As the main control in this system is the depth of indentation δ, we used this as an input parameter in our calculations rather than applied force.

The importance of the Poisson ratio was investigated by varying it, for the whole mesh, between 0.2 and 0.5, recalculating the radius of indentation accordingly and solving for the strain distribution with the new Poisson ratio with $E = 1$ kPa, $\delta = 1$ μm, and $R = 3$ μm. The depth of indentation was varied between 0.5 and 1.5 μm and the cellular strains resulting calculated with $E = 1$ kPa, $\nu = 0.3$, and $R = 3$ μm. The radius of the pipette was varied between 1 and 3 μm with $E = 1$ kPa, $\nu = 0.3$, and $\delta = 0.5$ μm.

Sensitivity of mechano-detection mechanisms

To investigate the sensitivity of the different mechano-detection mechanisms, we predicted the cellular strains used in mechanical stimulation studies by our and other groups, in which the detection mechanism was examined (Table 5). The strains were calculated as previously described assuming that all cell types have similar elasticities (reviewed in Lehenkari et al., 1999) and using $E = 1$ kPa for the micromanipulation studies.

Adaptation to mechanical strain

To examine the efficiency of increasing cellular elasticity to adapt to sustained mechanical strain, we changed the cellular material properties and examined the effect on cellular strain distributions. For whole cells, the material properties were increased by a given percentage. For the micromanipulation models of microbead pulling and twisting the elasticity was varied between 0.5 and 10 kPa. The effects of cellular elasticity on strain distributions due to micropipette poking were not assessed, as this technique offers no control over the force applied. However, a comparable study has been performed for AFM-indentation with spherical tips in Charras et al. (2001).

Cellular strain resulting from stray fluid flow

Based on results from studies by Schaffer et al. (1994) giving the substrate strains in a variety of stretching systems and Brown et al. (1998) giving the stresses resulting from stray fluid flow in those systems, we compared the cellular strains due to the intended stimulation (stretch) and those due to the unintended stimulation (fluid flow) using our FEM and CFD results. The fluid shear stresses induced by the three systems studied were two orders of magnitude lower than those commonly used to mechanically stimulate cells (2–5 Pa), and hence we ignored them. However, the fluid normal stresses reached significant magnitudes (up to 75 Pa). As cells are very close to being a flat surface, we approximated the normal stresses due to fluid flow by a hydrostatic pressure of similar magnitude.

Statistics and curve-fitting

Average, maximal, and median strains were compared with a Student's *t*-test and the results were deemed significant for $p < 0.05$. All curve-fitting was performed using Kaleidagraph (Synergy Software, Reading, PA) on a PC.

RESULTS

Experimentally measured material properties of osteoblasts

Topography and material properties (Fig. 1, *B* and *D*) were acquired using AFM. The cell was clearly identifiable as a softer area on a hard substrate (Fig. 1 *D*). The cellular elasticities varied between 1 kPa in the nuclear area and 100 kPa in the cytoplasmic skirt, and did not correlate with cell height (Fig. 1, *B* and *D*). Stress fibers could clearly be seen as "stiffer lines" spanning the cell from side to side (Fig. 1 *D*); these correlate with features in the AFM phase image (Fig. 1 *C*) and show a distribution similar to actin stress bundles identified with rhodamine-phalloidin staining (Fig. 1 *A*). The cellular elasticity frequency distribution for the 10 cells used fitted a Gaussian curve centered on 14 kPa (Fig. 1 *E*). Finite element models of the cells were created (for example, in Fig. 1 *F* from data in Fig. 1, *B* and *D*).

Strain distributions and magnitudes

Whole-cell models

Substrate stretch produced maximal strains along the axis of stretch. The strain distributions were very homogenous along the *x* axis with average and median absolute strains of 1030 $\mu\epsilon$, and maximal absolute strains of 1270 $\mu\epsilon$ (Table 1). Strains in the *y*- and *z*-directions were significantly lower than in the *x*-direction. Most of the cellular strains were close to the imposed stretch and higher strains were situated in the vicinity of stress fibers (Fig. 2 *A*). The evolution of maximum, median, and average absolute strains (averaged over 10 cells) could be predicted for commonly used values of substrate stretch (Fig. 2 *B*).

Intermittent hydrostatic pressure produced compressive strains that were maximal in the vertical direction (Table 1). The strain distribution was heterogeneous, with maximal strains sixfold higher than average or median strains (Fig. 3 *A* and Table 1). The maximally strained areas coincided with areas of lower elastic modulus (Figs. 1 *B* and 3 *A*), such as the nuclear region or areas of the cytoplasm devoid of stress fibers. The evolution of maximum, median, and av-

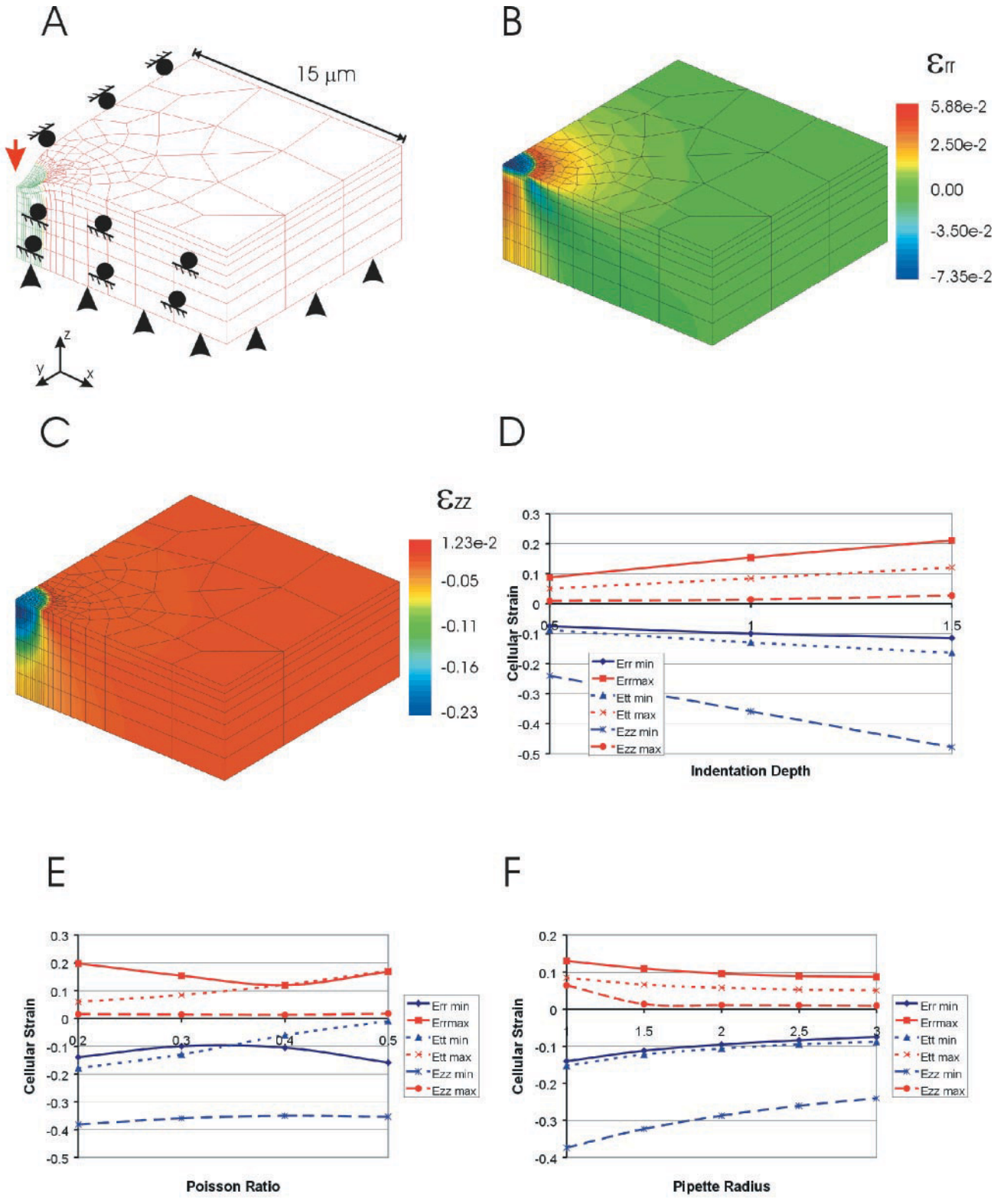

FIGURE 7 The effect of micropipette poking. (*A*) The cellular deformation amplified twofold resulting from micropipette poking for a 0.5 μm indentation. The micropipette is in contact with the top surface in the region in green. The red arrow indicates the direction of force application. Black triangles indicate where the substrate was fully constrained. The balls indicate a sliding boundary condition. (*B*) The radial strain distribution (ϵ_{rr}) resulting from micropipette poking. High tensile strains are present on the border of the indented region. (*C*) The vertical strain distribution (ϵ_{zz}) resulting from micropipette poking. High compressive strains are present under the area of indentation. (*D*) The evolution of cellular strains as a function indentation depth for a pipette radius of 3 μm. (*E*) The evolution of cellular strains with the Poisson ratio for a pipette radius of 3 μm. (*F*) The evolution of cellular strains with pipette radius.

TABLE 1 Strain magnitudes resulting from whole-cell mechanical stimulation

Stimulation	Average (abs(ε_{xx})) (in $\mu\varepsilon$)	Average (abs(ε_{yy})) (in $\mu\varepsilon$)	Average (abs(ε_{zz})) (in $\mu\varepsilon$)
Stretch (0.1%)	1030 ± 1.1	300 ± 1.1	308 ± 0.95
Hydrostatic pressure (5 Pa)	2.20 ± 0.69	2.14 ± 0.84	187 ± 45
Fluid flow (5 Pa)	2.19 ± 0.9	1.59 ± 0.6	199 ± 78
	Median (abs(ε_{xx}))	Median (abs(ε_{yy}))	Median (abs(ε_{zz}))
Stretch (0.1%)	1030 ± 23	307 ± 7.5	309 ± 9.2
Hydrostatic pressure (5 Pa)	0.002 ± 0.001	0.002 ± 0.001	164 ± 63
Fluid flow (5 Pa)	0.001 ± 0.001	0.001 ± 0.0006	92 ± 38.2
	Max (abs(ε_{xx}))	Max (abs(ε_{yy}))	Max (abs(ε_{zz}))
Stretch (0.1%)	1270 ± 26	366 ± 19	373 ± 16
Hydrostatic pressure (5 Pa)	44.3 ± 15	39.2 ± 20	699 ± 140
Fluid flow (5 Pa)	48.9 ± 23.4	35.7 ± 19.4	1080 ± 48

All values were averaged over the 10 cell models. Average, median, and maximum absolute strains are given for the diagonal elements of the strain tensor.

erage absolute strains (averaged over 10 cells) could be predicted for physiologically relevant pressures (Fig. 3 *B*). Values for higher hydrostatic pressures used in some setups can be extrapolated from the graph (Fig. 3 *B*). A pressure of 1 kPa would apply maximal vertical strains (ϵ_{zz}) of up to 14% and average vertical strains of 3.7%.

Fluid shear produced maximal strains in the vertical direction (Table 1). Maximal strains were 10-fold higher than average or median strains, pointing to a heterogeneous strain distribution (Table 1 and Fig. 4 *B*). The vertical fluid shear stresses (τ_z, Fig. 4 *A*) were lower upstream, where pressure build-up counters the traction force due to shear stresses, and larger downstream, where shear stresses and pressure have additive effects. The vertical cellular strains (Fig. 4 *B*) were tensile and maximal downstream from the cell apex, in areas with a low elastic modulus that coincided with the location of the nucleus. Maximal, average, and median strains (averaged over 10 cells) could be calculated for commonly used values of shear stress (Fig. 4 *C*).

The maximal strains exerted by the three modes of stimulation were close to one another with a 0.1% stretch producing maximal absolute strains of 1270 $\mu\epsilon$, a 5 Pa hydrostatic pressure producing maximal absolute strains of 700 $\mu\epsilon$, and a 5 Pa shear stress producing maximal absolute strains of 1080 $\mu\epsilon$ (Table 1). Fluid flow and hydrostatic pressure exerted significantly different maximum and median vertical strains ($p = 0.04$ and $p = 0.01$), but not average vertical strains ($p = 0.70$). Maximal absolute vertical strains due to fluid flow were significantly lower than the maximal absolute horizontal strains produced by substrate stretch ($p < 0.001$).

Micromanipulation models

For commonly used values of the stimuli and an elasticity of 1 kPa, the micromanipulation techniques applied strains in excess of 5%, which was on average one order of magnitude higher than those applied by whole-cell techniques (Tables 1 and 2). The radial strain distribution (ϵ_{rr}) for microbead pulling (Fig. 5 *B*) showed the presence of high tensile and short-range surface strains at the border between the region tethered to the bead and the free region (Fig. 5 *A*). The cellular strains increased linearly with applied force (Fig. 5 *E*). The maximal vertical strains were the largest strain component, followed by the maximal radial strains (Fig. 5 *E*).

The horizontal strain distribution (ϵ_{xx}) for microbead twisting (Fig. 6 *B*) showed the presence of high tensile strains on the surface on either side of the border between the region where the bead is bound to the cell and the free region (Fig. 6 *A*). The cellular strains increased quasi-linearly with increasing angular motion (Fig. 6 *C*). Maximal and minimal values for each strain component were of similar magnitude (Fig. 6 *C*). The bead radius, and hence the

TABLE 2 Strain magnitudes resulting from micromanipulation

Stimulation Method	$\varepsilon_{rr}/\varepsilon_{xx}$		$\varepsilon_{tt}/\varepsilon_{yy}$		ε_{zz}	
	min (%)	max (%)	min (%)	max (%)	min (%)	max (%)
Micropipette poking, $R = 3$ μm, $\delta = 0.5$ μm	−7.5	8.7	−8.8	5.0	−24	0.94
Bead pulling, $E = 1$ kPa, $F = 4$ pN	−1.0	2.1	−0.74	0.6	−0.19	5.7
Bead twisting, $E = 1$ kPa, $p = 4$ Pa	−1.5	1.4	−0.54	0.58	−7.3	7.3

The parameters pertaining to each study are given in the table. ε_{rr} and ε_{tt} are given for micropipette poking and microbead pulling, whereas ε_{xx} and ε_{yy} are given for the microbead twisting.

radius of indentation, only had a marginal effect on cellular strains (data not shown).

The radial strain distribution (ϵ_{rr}) (Fig. 7 *B*) for micropipette poking showed a large tensile component on the surface at the border between the indented and free region (Fig. 7 *A*). The vertical strain distribution (ϵ_{zz}) (Fig. 7 *C*) showed a large compressive component under the indented region. The cellular strains varied linearly with indentation depth (Fig. 7 *D*).

Effect of material property changes

Whole-cell models

When substrate stretch was applied, a twofold increase in the cellular elasticities had no influence on the strains exerted on the cell (change $<0.1\%$, Fig. 2 *D*). However, when the cellular elasticities were increased twofold and hydrostatic pressure or fluid shear were applied, the cellular strains were reduced by 50 and 33%, respectively (Figs. 3 *C* and 4 *D*).

Micromanipulation models

For microbead pulling and twisting, all components of cellular strain decreased dramatically with increasing elasticity (Figs. 5 *C* and 6 *F*, respectively) for a fixed stimulus. These decreases fitted well with a power-law ($r^2 > 0.95$ except "ϵ_{zz} min" for microbead pulling).

In microbead pulling experiments the vertical displacement of the bead for a force of 4 pN decreased from 21 nm for $E = 0.5$ kPa to 2.8 nm for $E = 10$ kPa. The vertical displacement as a function of elasticity fitted well with a power-law ($r^2 = 0.99$, Fig. 6 *F*).

During microbead twisting, the angular rotation of the bead for a pressure of 4 Pa decreased from 12° for $E = 0.5$ kPa to 1.5° for $E = 10$ kPa. The angular motion as a function of elasticity fitted well with a power-law ($r^2 = 0.99$, Fig. 5 *E*).

Effect of Poisson ratio changes

Whole-cell models

When substrate stretch was applied, the Poisson ratio had little effect on average or median strains. ϵ_{xx} was reduced by only 15% when ν was changed from 0.2 to 0.5 (Fig. 2 *E*). However, in models of hydrostatic pressure (Fig. 3 *D*) or fluid shear (similar evolution to Fig. 3 *D*, data not shown), the Poisson ratio was an important factor and it reduced the maximal, median, and average maximal strains by 93% when it was varied from 0.2 to 0.5. This is due to the predominantly compressive nature of these mechanical stimulations.

Micromanipulation models

The Poisson ratio had little influence on the order of magnitude in microbead pulling experiments (Fig. 5 *D*). The maximal radial and tangential strain decreased by 85% when ν was varied between 0.2 and 0.5. The two largest strain components in absolute value "ϵ_{zz} max" and "ϵ_{rr} min" varied by -56% and $+74\%$, respectively, when ν was changed from 0.2 to 0.5.

The magnitude of strains elicited by micropipette poking was not very sensitive to changes in Poisson ratio (Fig. 7 *E*). The maximal radial strains (ϵ_{rr}) were reduced by a maximum of 40% and the maximal tangential strains (ϵ_{tt}) by 94% when ν was varied from 0.2 to 0.5. In microbead twisting experiments (Fig. 6 *D*), the Poisson ratio had a dramatic influence around $\nu = 0.4$ where all components of strain were amplified to an order of magnitude above their value for other values of ν.

Effect of the direction of application of stimulus

In substrate stretch models, the stretch direction had no effect on the maximal strain (ϵ_{11} along the direction of stretch) introducing only a 7% variation in its magnitude (Fig. 2 *C*). In fluid shear models, rotating the direction of flow by 90° increased the maximal vertical strain (ϵ_{zz}) by 12% and reduced the average and median vertical strains by 5 and 8%, respectively (data not shown).

Effect of fluid flow parameters

The cellular strains varied linearly with the value of the cinematic viscosity μ (Fig. 4 *E*). Increasing cell height by 100% increased the maximal strains by only 7% (Fig. 4 *F*).

Osteocytes

Osteocytes embedded in a block of matrix compressed by 0.1% (1000 $\mu\epsilon$) were submitted to maximal vertical strains (ϵ_{zz}) of up to 1% (10,000 $\mu\epsilon$, Table 3). Hence, cellular strains were amplified 10-fold compared to matrix strains. Average and median vertical strains were 2-fold larger than cellular strains in the direction of stretch (ϵ_{xx}).

Cellular strain elicited by stray fluid flow

The cellular strains elicited by stray fluid flow induced additional average cellular strains of up to 2810 $\mu\epsilon$ (0.28%) and maximal cellular strains of up to 10,500 $\mu\epsilon$ (1.05%), which represented respectively 13% and 39% of the strains induced by substrate stretch (Flexercell system, Table 4). The MIT system induced average additional strains of 4% and maximal strains of 14% of the value imposed by substrate stretch. The fluid flow-induced strains reached 1420

TABLE 3 Strain magnitudes in an osteocyte embedded in the bone matrix

Osteocyte	abs(ε_{xx}) ($\mu\varepsilon$)	abs(ε_{yy}) ($\mu\varepsilon$)	abs(ε_{zz}) ($\mu\varepsilon$)
Average	1100	300	2000
Median	1000	300	2000
Maximum	2400	800	10,000

$\mu\epsilon$ (0.14%) on average and a maximum of 5310 $\mu\epsilon$ (0.53%) in the Providence system.

DISCUSSION

In this paper we combine AFM measurements of elasticities and profiles of live osteoblasts with CFD and FEM to predict, for the first time, the cellular strain distributions resulting from common whole-cell stimulation methods, such as substrate stretch, intermittent hydrostatic pressure application, or fluid shear. In addition, we give the strain distributions resulting from mechanical stimulation by micromanipulation techniques, such as microbead pulling, microbead twisting, or micropipette poking. In all cases we examined the effect of the relevant mechanical parameters on the strain distributions, and provide the magnitudes of cellular strains for commonly used values of the control parameters for each of the experimental conditions. We have examined, for each experimental condition, whether increasing cellular material properties may be a good strategy for adapting to sustained mechanical strain, by assessing the impact of this modification upon the cellular strain distributions. By combining our modeling data with experimental data from other groups (Table 5), we examine the magnitudes of strains needed to activate different strain detection mechanisms. We also underline the necessity to design new substrate stretching devices that reduce stray fluid flow. We believe that this work will help further our understanding of cellular detection of, and adaptation to, mechanical strain.

Cellular strain detection mechanisms

Cells can detect strains through a variety of mechanisms that, as a first step, involve stretch-activated cation channels, integrin transmembrane receptors, G-proteins, or tyrosine kinases (Sachs and Morris, 1998; Gudi et al., 1998; Banes et al., 1995; Malek and Izumo, 1996). The threshold strain of activation and the strain component to which they are sensitive may be different. We examined experiments performed by other groups investigating the mechanisms involved in the detection of mechanical stimulation and calculated the strain distributions that they applied (Table 5).

All of the micromanipulation techniques had both a high radial tensile component (>1%) on the cell surface (Figs. 5 *B*, 6 *B*, 7 *B*), compatible with a membrane stretch detection mechanism (Table 5). The large vertical component (>5%) (tensile for microbead pulling, mixed for microbead twisting, and compressive for micropipette prodding; Fig. 7 *C*) could be detected by cytoskeleton-based mechanisms, such as via tyrosine kinases (Glogauer et al., 1997; Chen et al., 2001). Furthermore, most groups report inhibition of cellular reactions when exposed to stretch-activated channel blocking agents, Gd^{3+} (Sachs and Morris, 1998), or *Grammostola spatulata* venom (Suchyna et al., 2000). However, the possibility that the high levels of strain applied by these techniques over very small areas induce cell damage or membrane rupture should not be excluded, especially in the case of micropipette prodding.

Detection of mechanical stimuli in cells subjected to intermittent hydrostatic pressure have been reported to involve stretch-activated channels and integrins (Lee et al., 2000). The magnitude of the in-plane strains resulting from hydrostatic pressure was similar to that resulting from micromanipulation techniques, and hence the detection may be mediated by stretch-activated channels.

Reported detection mechanisms for substrate stretch are varied and are thought to involve stretch-activated channels, tyrosine kinases, integrins, and the cytoskele-

TABLE 4 Additional cellular strains induced by stray fluid flow in experimental substrate stretch systems

Loading system	Applied Stretch	Fluid pressure (Pa)	Shear stress (Pa)	Nominal ε_{xx} (%)	Nominal ε_{yy} (%)	Nominal ε_{zz} (%)	Additional ε_{xx} (%)	Additional ε_{yy} (%)	Additional ε_{zz} (%)
Average Cellular Strain									
Flexercell	2.1%*	75†	0.04†	2.16	0.63	0.65	0.003	0.003	0.28
Providence system	NA	−38†	0.05†	NA	NA	NA	0.001	0.002	0.14
M.I.T system	3.0%*	−40†	0.05†	3.09	0.90	0.92	0.001	0.002	0.15
Maximal Cellular Strain									
Flexercell	2.1%*	75†	0.04†	2.67	0.77	0.78	0.066	0.059	1.05
Providence system	NA	−38†	0.05†	NA	NA	NA	0.034	0.030	0.53
M.I.T system	3.0%*	−40†	0.05†	3.81	1.10	1.12	0.035	0.031	0.56

The nominal strains result from substrate stretch. The additional strains result from stray fluid flow.
*From Schaffer et al. (1994).
†From Brown et al. (1998).

TABLE 5 Pathway for detection of mechanical strain and strain magnitudes applied

Stimulation	Authors	Cell Type	Readout*	Reagents Used
Atomic force microscopy	Charras et al., 2002	osteoblasts	Ca^{2+}	Gd^{3+}, thapsigargin, calcium-free medium, genistein, verapamil, PLC-inhibitor
Microbead pulling	Glogauer et al., 1997 and 1995	osteoblasts	Ca^{2+}	genistein, BAPTA, Gd^{3+}, EGTA, Mn^{2+}
	Niggel et al., 2000	endothelial cells	Ca^{2+}	Gd^{3+}, Mn^{2+}
	Niggel et al., 2000	glioma cells	Ca^{2+}	EGTA, thapsigargin, calcium-free medium, Mn^{2+}
Microbead twisting	Chen et al., 2001	endothelial cells	Endothelin 1 mRNA	Gd^{3+}, EGTA, genistein, myosin inhibitor
Micropipette poking	Xia and Ferrier, 1992	osteoblasts	Ca^{2+}	calcium-free medium, cocktail: Gd^{3+} + verapamil + nifedipine + Co^{2+}
	Guilak et al., 1994	chondrocytes	Ca^{2+}	Calcium-chelation, Gd^{3+}, amiloride, verapamil, nifedipine
	Hu and Sachs, 1996	chick heart cells	Electrophysiology	Gd^{3+}, spider venom
	Diamond et al., 1994	endothelial cells	Ca^{2+}	amiloride, nifedipine, PLC-inhibitor, TEA
Hydrostatic pressure	Lee et al., 2000	chondrocytes	Electrophysiology	Gd^{3+}, antibodies to integrins, genistein
	Salter et al., 1997	osteoblasts	Electrophysiology	Gd^{3+}, antibodies to integrins, genistein
Substrate stretch	Toma et al., 1997	osteoblasts	Osteopontin mRNA	genistein, quercetin, chelerythrine, cyclohexamide, H89
	Rosales et al., 1997	endothelial cells	Ca^{2+}	Gd^{3+}, calcium-free medium
	Hayakawa et al., 2001	aorta and kidney cell lines	Stress fiber realignment	Gd^{3+}
	Peake et al., 2000	osteoblastic cell line, MC3T3	c-fos mRNA	Gd^{3+}, nifedipine, EGTA, β1 integrin antibody
Fluid shear stress	McAllister and Frangos, 1999	osteoblasts	NO production	calcium chelation, G-protein inhibition
	Ryder et al., 2001	osteoblasts	Ca^{2+}	Gd^{3+}, nifedepine
	Sakai et al., 1998	osteoblast cell line SaOs-2	TGF-β1 mRNA	Gd^{3+}, verapamil
	Malek and Izumo, 1996	endothelial cells	Cell shape change and stress fiber induction	Gd^{3+}, genistein, chelerythrine, calcium chelator, herbymycin
	Hung et al., 1995	osteoblasts	Ca^{2+}	Gd^{3+}, verapamil, neomycin, calcium-free medium, TMB-8
	Yellowley et al., 1999	chondrocytes	Ca^{2+}	Gd^{3+}, thapsigargin, neomycin
	You et al., 2001	osteoblasts	Ca^{2+}	Gd^{3+}, thapsigargin, nifedipine, U73122
	Ajubi et al., 1999	osteocytes	PGE2 release	Gd^{3+}, EGTA, TEA, calcium chelation, thapsigargin, PLC-inhibitor
	Reich et al., 1997	osteoblasts	Ca^{2+}	calcium chelation (EGTA, Quin2), G-protein inhibition

*Readout gives the parameter on which the effects of inhibitors is tested.
†Abbreviations: SAC, stretch activated channels; TK, tyrosine kinases; PLC, phospholipase C; IP3, inositol-1,4,5-triphosphate; PKA, protein kinase A; VACC, voltage activated calcium channel; PGE2, prostaglandin E2; NO, nitric oxide.

ton (Table 5). FE models revealed that the cells were subjected to strains close to those imposed on the substrate (in agreement with experimental data by Caille et al., 1998) and, for the experiments reported in Table 5

Intracellular pathway†	Stimulus	Subtype	Max(εxx/εrr)	Max(εyy/εtt)	Max(εzz)
SAC and IP3	$F > 10$ nN		3%	3%	9%
SAC and TK	$F = 4$ pN		2%	0.60%	5.00%
SAC	$F = 4$ pN		2%	0.60%	5.00%
IP3, SAC			2%	0.60%	5.00%
SAC, TK and cytoskeletal tension	$p = 2$ Pa		0.70%	0.25%	3.60%
SAC and VACCs	NA		>8%	>8%	>24%
SAC	$\delta = 1$–2 um		21%	12%	47%
SAC	$\delta = 3.8$ um	rounded cell	>21%	>12%	>47%
PLC	NA		>8%	>8%	>24%
SAC and integrins	$p = 13$ kPa	intermittent	11%	10%	182%
SAC and integrins	$p = 13$ kPa	intermittent	11%	10%	182%
TK, PKA, cytoskeleton	$\varepsilon_{xx} = 1.3\%$	uniform biaxial, flexercell	1.30%	1.30%	?
SAC and IP3	$\varepsilon_{xx} = 10\%$	uniform biaxial, flexercell	10%	?	?
SAC and cytoskeleton	$\varepsilon_{xx} = 20\%$	uniaxial	20%		
SAC, VACCs and integrins	$\varepsilon_{xx} = 0.1\%$	4 point bending	0.10%		
G-protein and extracellular Ca	$\tau = 2.6$ Pa	steady	25 $\mu\varepsilon$	18 $\mu\varepsilon$	520 $\mu\varepsilon$
SAC and VACCs	$\tau = 2.5$ Pa	steady	24 $\mu\varepsilon$	17 $\mu\varepsilon$	500 $\mu\varepsilon$
SAC and VACCs	$\tau = 2$ Pa	steady	19 $\mu\varepsilon$	13 $\mu\varepsilon$	400 $\mu\varepsilon$
TK, PLC	$\tau = 2$ Pa	steady	19 $\mu\varepsilon$	13 $\mu\varepsilon$	400 $\mu\varepsilon$
SAC and PLC	$\tau = 3.5$ Pa	steady	34 $\mu\varepsilon$	24 $\mu\varepsilon$	700 $\mu\varepsilon$
PLC and G-protein	$\tau = 2$ Pa	oscillatory	19 $\mu\varepsilon$	13 $\mu\varepsilon$	400 $\mu\varepsilon$
IP3 and VACCs	$\tau = 2$ Pa	oscillatory	19 $\mu\varepsilon$	13 $\mu\varepsilon$	400 $\mu\varepsilon$
SAC, VACCs and PLC	$\tau = 0.7 \pm 0.3$	pulsating	9.6 $\mu\varepsilon$	6.8 $\mu\varepsilon$	200 $\mu\varepsilon$
G-proteins, extracellular calcium	$\tau = 2.4$ Pa	steady	23 $\mu\varepsilon$	16 $\mu\varepsilon$	480 $\mu\varepsilon$

(except Peake et al., 2000), the strain magnitude was similar to that detected by stretch-activated channels or tyrosine kinases in micromanipulation experiments. Furthermore, recent studies point toward the detection of substrate stretch through mechano-sensitive channels activated by intercellular tension applied through adherens-junctions (Ko et al., 2001). In contrast, some experiments report effects of substrate stretch on osteoblasts for low

strains, around 0.1% (Peake et al., 2000; Zaman et al., 1997; Fermor et al., 1998).

However, one must be circumspect when interpreting substrate stretch data, as many systems also induce stray fluid flow (Table 4 and Brown et al., 1998; You et al., 2000). Indeed, the maximal cellular strains induced by stray fluid flow reached 40% of the value applied by substrate stretch (Table 5); hence, cellular reactions obtained in such systems may be mediated not only by substrate stretch, but also by fluid flow. Owan et al. (1997) showed that the stray fluid flow resulting from a four-point bending system (such as that used by Peake et al., 2000) was sufficient to elicit cellular reactions. This underlines the necessity of designing new substrate stretch systems (e.g., You et al., 2000) and may explain differences in results between systems that elicit large stray fluid flow and those that do not.

In fluid shear stress experiments an equal number of groups have reported mechanisms involving, or not involving, stretch-activated cation channels for similar values of fluid shear. The strain levels for fluid shear experiments, and in particular the in-plane strains, which may be detected by stretch-activated channels, are two to three orders of magnitude lower than those elicited by other stimulation techniques. Hence, either the stretch-activated cation channels are particularly sensitive to fluid shear or another mechanism is utilized. Recently, it has been shown that G-proteins reconstituted within phospholipid vesicles increased their GTPase activity in response to fluid shear (Gudi et al., 1998). GTPase activity also increased with increasing vesicle membrane fluidity. During fluid shear, cell membrane fluidity in living cells increased with the onset of fluid flow in the upstream cellular region (Butler et al., 2001). Taken together with the very low magnitudes of strain induced and the nonspecificity of Gd^{3+} (Sachs and Morris, 1998), these data may point toward a detection mechanism relying on an increase in membrane fluidity detected by G-proteins with Gd^{3+} having an effect on mechanisms downstream from these.

In summary, whereas, for commonly used values of the parameters, most stimulation methods elicited strains of comparable magnitude, fluid shear experiments generated far lower cellular strains and may trigger an entirely different detection mechanism. Moreover, several mechanisms may co-exist on each cell type and be sensitive to different components of the strain distribution. Chen et al. (2001) and Glogauer et al. (1997) report that stretch-activated channels and tyrosine kinases act cooperatively to mediate responses to microbead twisting and pulling. Hayakawa et al. (2001) report that whereas stretch-activated channels govern whole-cell reorientation in response to substrate stretch, they do not seem to be involved in the reorientation of actin stress fibers within the cell. Such co-existence of detection mechanisms may be beneficial to the cell in fine tuning cellular responses, such as the transcription of different genes to various ranges of cellular strain.

Importance of the cellular Poisson ratio

The cellular Poisson ratio remains unknown, though experiments by Maniotis et al. (1997) report a Poisson ratio of 0.25 ± 0.05. The Poisson ratio had little influence on the magnitude of strains exerted in microbead pulling, micropipette poking, or substrate stretch experiments (Figs. 2 *E*, 5 *D*, 7 *E*). However, it was of crucial importance in hydrostatic compression or fluid shear experiments (Fig. 3 *D* and data not shown), which apply predominantly compressive stresses. When the cell tended to incompressibility, the magnitude of cellular strains was greatly reduced. Interestingly, for microbead twisting experiments, the Poisson ratio appeared to have a dramatic effect around $\nu = 0.4$, where the strains elicited were increased by one order of magnitude. These results are of particular interest as cells may be able to modulate their Poisson ratio by altering their intracellular architecture. In support of this, Maniotis et al. (1997) showed that specific disruption of cytoskeletal fibers increased the cellular Poisson ratio to $\sim$0.5, bringing the cell closer to an incompressible gel.

Cellular adaptation to mechanical perturbation

Cellular adaptation to mechanical stimuli has been reported in many instances, and our study may explain how those adaptations help the cell withstand sustained mechanical stimulation. When exposed to fluid shear stress, cells and their F-actin stress fibers realign with the direction of flow (Girard and Nerem, 1993). Furthermore, cells submitted to sustained flow have higher elasticities than unstrained cells (Sato et al., 2000). Realignment of the cell body with the direction of flow serves to reduce the shear stresses (-5%) acting on the cell (Barbee et al., 1995) and increasing the cellular material properties reduces the strains to which the cell is subjected (-50%, Fig. 4 *D*). In cells subjected to a long period of microbead pulling, Glogauer et al. (1997) reported the formation of actin plaques, with higher elasticities under the microbeads. Our study shows that increasing cellular elasticity in response to microbead stimulation is a very efficient method for reducing cellular strains (Fig. 5 *C*). Furthermore, addition of actin need only be restricted to a small area because the radial strains decay very rapidly (Fig. 5 *B*). Similarly, our models predict that cells exposed to long periods of increased intermittent hydrostatic pressure could counter the increased strains by increasing their elasticity. In agreement with this, cardiomyocytes from animals with cardiac pressure overload had elasticities twofold higher than those from control animals (Tagawa et al., 1997). However, several groups report a complete disassembly of the cytoskeleton in response to intermittent hydrostatic pressure (Haskin et al., 1993; Parkkinen et al., 1995), though this may be due to the excessive magnitude of the pressure applied ($>$4 MPa). Indeed, to reduce the in-plane strains to values below 1% for a 4 MPa pressure, the

cell would need to increase its elasticity by several orders of magnitude. Hence, a different mechanism of adaptation may be necessary and disassembly of the cytoskeleton could be the first step. There is evidence that cytoskeletal tensegrity enables cells to accommodate changes in volume (Guilak, 1994) giving them a continuum scale Poisson ratio that is not 0.5 (Maniotis et al., 1997 report a value of 0.25 ± 0.05). Disassembly of the cytoskeleton would change the cell into a fluid surrounded by a lipid bilayer; this would make it quasi-incompressible, thereby drastically reducing the magnitude of strains to which it would be subjected (Maniotis et al., 1997; Fig. 3 *D*). In substrate stretch experiments, cellular elasticity had little influence on cellular strains (Fig. 2 *D*). This is due to the fact that the cells are tethered to the substrate (Fig. 1 *A*) and hence any displacement imposed on the substrate is imposed on the cells. In this case, it is important to consider the discrete, rather than continuum, nature of the cell cytoskeleton. Indeed, the cell is only anchored to its substrate at a number of discrete points (focal adhesion complexes, shown in green, Fig. 1 *A*) that often coincide with the extremities of the cellular actin stress fibers (shown in red, Fig. 1 *A*). If the fibers run along the direction of stretch, the distance between the two extremities will be increased and the fibers will exert a vertical compression on the underlying structures. In contrast, if the fibers reorganize such that they run perpendicular to the direction of stretch, the distance between the two extremities stays unchanged and no compression is applied (Hayakawa et al., 2001). Thus, cellular adaptation can be explained in terms of cytoprotective responses geared at shielding the cell from unusual strain magnitudes (Ko and McCulloch, 2000).

Strain detection in osteocytes

The strains to which osteocytes were subjected reached 1% and were an order of magnitude larger than the strain imposed on the matrix (Table 3), confirming earlier results by Riemer-McReady and Hollister (1997). Based on micromanipulation studies and our estimates of the cellular strains resulting from these, this magnitude of strain would be sufficient to activate stretch-activated cation channels (Table 5). However, there is still much debate as to the nature of the stimulus to which osteocytes respond. Predicted loading-induced shear stresses in the osteocyte lacunae (0.8–3 Pa, Weinbaum et al. (1994)) have been found to have excitatory effects on osteocytes in vitro (You et al., 2000; Ajubi et al., 1999). However, in cyclically loaded bone explants, Gd^{3+} abolished loading-related increases in nitric oxide and prostaglandin PGI_2 (Rawlinson et al., 1996), which would point to a mechanism mediated by stretch-activated channels. However, the same group (Rawlinson et al., 2000) also showed that pertussis toxin, a blocker of G-proteins, inhibits loading-related increases in prostaglandins PGE_2 and PGI_2, thus pointing to a detection of the fluid flow within the bone. Hence, both signaling mechanisms could realistically be involved and may co-exist in osteocytes to mediate the detection of, and responses to, bone deformation.

Limitations of the integrated measurement and modeling process

Combining AFM measurements with modeling techniques has enabled us to compare the strains elicited by different straining techniques for the first time. However, there are a number of limitations to this approach. First, we have modeled the cellular material as being linear elastic. This is an acceptable starting point as we were interested only in the static solutions to mechanical stimulation (Zhu et al., 2000; Charras et al., 2001). However, cells are viscoelastic (Wu et al., 1998) and the viscoelastic components of their response to mechanical strain may be important in the detection, or transduction, of mechanical stimuli. Furthermore, the tensegrity-architecture of the cytoskeleton of living cells exhibits strain hardening (Chen et al., 2001; Ingber, 1993). Ignoring this factor may lead to an overestimation of the strains applied. This may be particularly important in the case of stimulation through integrins or transmembrane proteins that are tethered to the cytoskeleton, as occurs in microbead pulling or twisting. Thus, we consider that a new finite element formulation, based on the behavior of a basic tensegrity unit subjected to mechanical forces (Stamenovic et al., 1996), will need to be created for the realistic modeling of cells. Second, we assumed that the cells were uniformly attached to the cell surface. This is clearly not the case (Fig. 1 *A*) and cells exposed to substrate stretch have been shown to upregulate focal adhesion complex sizes in response to loading (Wozniak et al., 2000). Discrete attachment points onto the substrate may give rise to more complex cellular deformations and strain distributions on the underside of cells when exposed to substrate stretch, fluid shear, or hydrostatic pressure. Third, in our models we used the elasticities of subconfluent cells, which may have different material property distributions than confluent cells. Fourth, in our studies we have assumed, based on studies by Maniotis et al. (1997), that cells had Poisson ratios between 0.2 and 0.5. Recently, materials with Poisson ratios that are negative or larger than 0.5 have been discovered. Taken together, these limitations to the modeling process performed in this paper indicate that future studies will require new and more complex, and hence more computing time-intensive, techniques to model realistic situations.

CONCLUSIONS

In summary, we have used AFM in conjunction with FEM and CFD to predict the cellular strain distributions resulting from common whole-cell mechanical stimulation tech-

niques. Furthermore, we also predict the strain distributions resulting from micromanipulation techniques. These data will enable direct comparison of downstream events resulting from different stimulation techniques and help understand whether different mechanical stimulations exerting similar strain levels are detected through distinct pathways. Cellular adaptation responses to mechanical strain were simulated and explained in terms of cell mechanics and cytoprotection. We believe that the application and future developments of in silico cell modeling will help understand the interplay among mechanical forces, strain detection, gene expression, and cellular adaptation in physiology. Diseases commonly occur in organs/tissues exposed to mechanical stresses, such as osteoporosis in bone and atherosclerosis in blood vessels. A greater understanding of the interplay of modifications in the mechanical forces with other etiological factors may help further our understanding of the pathogenesis of a range of common diseases.

The authors thank Thierry Charras (CEA, France), Jean-Paul Magnaud (CEA, France), and Florent Cayré (Snecma, France) for their help with the modeling and their careful reading of the manuscript.

This work was supported by a Johnson and Johnson "Focused Giving" award and by a program grant from The Wellcome Trust (to M.A.H.).

REFERENCES

A-Hassan, E., W. F. Heinz, M. D. Antonik, N. P. D'Costa, S. Nageswaran, C.-A. Schoenenberger, and J. H. Hoh. 1998. Relative microelastic mapping of living cells by atomic force microscopy. *Biophys. J.* 74: 1564–1578.

Ajubi, N. E., J. Klein-Nulend, M. J. Alblas, E. H. Burger, and P. J. Nijweide. 1999. Signal transduction pathways involved in fluid flow-induced PGE2 production by cultured osteocytes. *Am J. Physiol. Endocrinol. Metab.* 276:E171–E178.

Banes, A. J., M. Tsuzaki, J. Yamamoto, T. Fischer, B. Brigman, T. Brown, and L. Miller. 1995. Mechanoreception at the cellular level: the detection, interpretation, and diversity of responses to mechanical signals. *Biochem. Cell Biol.* 73:349–365.

Barbee, K. A., T. Mundel, R. Lal, and P. F. Davies. 1995. Subcellular distribution of shear stress at the surface of flow-aligned and nonaligned endothelial monolayers. *Am. J. Physiol. Heart Circ. Physiol.* 268: H1765–H1772.

Brown, T. D., M. Bottlang, D. R. Pedersen, and A. J. Banes. 1998. Loading paradigms—intentional and unintentional—for cell culture mechanostimulus. *Am. J. Med. Sci.* 316:162–168.

Butler, P. J., G. Norwich, S. Weinbaum, and S. Chien. 2001. Shear stress induces a time- and position-dependent increase in endothelial cell membrane fluidity. *Am. J. Physiol. Cell Physiol.* 280:C962–C969.

Caille, N., Y. Tardy, and J. J. Meister. 1998. Assessment of strain field in endothelial cells subjected to uniaxial deformation of their substrate. *Ann. Biomed. Eng.* 26:409–416.

Charras, G. T., and M. A. Horton. 2002. Single cell mechanotransduction and its modulation analyzed by atomic force microscope microindentation. *Biophys. J.* 82:2970–2981.

Charras, G. T., P. P. Lehenkari, and M. A. Horton. 2001. Atomic force microscopy can be used to mechanically stimulate osteoblasts and evaluate cellular strain distributions. *Ultramicroscopy.* 86:85–95.

Chen, J., B. Fabry, E. L. Schiffrin, and N. Wang. 2001. Twisting integrin receptors increases endothelin-1 gene expression in endothelial cells. *Am. J. Physiol. Cell Physiol.* 280:C1475–C1484.

Currie, I. G. 1993. Fundamental Mechanics of Fluids. McGraw-Hill, New York.

Diamond, S. L., F. Sachs, and W. J. Sigurdson. 1994. Mechanically induced calcium mobilization in cultured endothelial cells is dependent on actin and phospholipase. *Arterioscler. Thromb.* 14:2000–2006.

Drury, J. L., and M. Dembo. 1999. Hydrodynamics of micropipette aspiration. *Biophys. J.* 76:110–128.

Fermor, B., R. Gundle, M. Evans, M. Emerton, A. Pocock, and D. Murray. 1998. Primary human osteoblast proliferation and prostaglandin E2 release in response to mechanical strain in vitro. *Bone.* 22:637–643.

Girard, P. R., and R. M. Nerem. 1993. Endothelial cell signaling and cytoskeletal changes in response to shear stress. *Front Med. Biol. Eng.* 5:31–36.

Glogauer, M., P. Arora, G. Yao, I. Sokholov, J. Ferrier, and C. A. McCulloch. 1997. Calcium ions and tyrosine phosphorylation interact coordinately with actin to regulate cytoprotective responses to stretching. *J. Cell Sci.* 110:11–21.

Glogauer, M., and J. Ferrier. 1998. A new method for application of force to cells via ferric oxide beads. *Pflugers Arch.* 435:320–327.

Glogauer, M., J. Ferrier, and C. A. McCulloch. 1995. Magnetic fields applied to collagen-coated ferric oxide beads induce stretch-activated Ca2+ flux in fibroblasts. *Am. J. Physiol. Cell Physiol.* 269: C1093–C1104.

Gu, W. Y., W. M. Lai, and V. C. Mow. 1997. A triphasic analysis of negative osmotic flows through charged hydrated soft tissues. *J. Biomech.* 30:71–78.

Gudi, S., J. P. Nolan, and J. A. Frangos. 1998. Modulation of GTPase activity of G proteins by fluid shear stress and phospholipid composition. *Proc. Natl. Acad. Sci. U.S.A.* 95:2515–2519.

Guilak, F. 1994. Volume and surface area measurement of viable chondrocytes in situ using geometric modeling of serial confocal sections. *J. Microsc.* 173:245–256.

Guilak, F., and V. C. Mow. 2000. The mechanical environment of the chondrocyte: a biphasic finite element model of cell-matrix interactions in articular cartilage. *J. Biomech.* 33:1663–1673.

Hansen, J. C., R. Skalak, S. Chien, and A. Hoger. 1996. An elastic network model based on the structure of the red blood cell membrane skeleton. *Biophys. J.* 70:146–166.

Haskin, C., I. Cameron, and K. Athanasiou. 1993. Physiological levels of hydrostatic pressure alter morphology and organization of cytoskeletal and adhesion proteins in MG-63 osteosarcoma cells. *Biochem. Cell Biol.* 71:27–35.

Hayakawa, K., N. Sato, and T. Obinata. 2001. Dynamic reorientation of cultured cells and stress fibers under mechanical stress from periodic stretching. *Exp. Cell Res.* 268:104–114.

Hu, H., and F. Sachs. 1996. Mechanically activated currents in chick heart cells. *J. Membr. Biol.* 154:205–216.

Hung, C. T., F. D. Allen, S. R. Pollack, and C. T. Brighton. 1996. Intracellular Ca2+ stores and extracellular Ca2+ are required in the real-time Ca2+ response of bone cells experiencing fluid flow. *J. Biomech.* 29:1411–1417.

Ingber, D. E. 1993. Cellular tensegrity: defining new rules of biological design that govern the cytoskeleton. *J. Cell Sci.* 104:613–627.

Johnson, K. L. 1985. Contact Mechanics. Cambridge University Press, Cambridge, New York, Melbourne.

Jortikka, M. O., J. J. Parkkinen, R. I. Inkinen, J. Karner, H. T. Jarvelainen, L. O. Nelimarkka, M. I. Tammi, and M. J. Lammi. 2000. The role of microtubules in the regulation of proteoglycan synthesis in chondrocytes under hydrostatic pressure. *Arch. Biochem. Biophys.* 374:172–180.

Ko, K. S., P. D. Arora, and C. A. McCulloch. 2001. Cadherins mediate intercellular mechanical signaling in fibroblasts by activation of stretch-sensitive calcium-permeable channels. *J. Biol. Chem.* 276:35967–35977.

Ko, K. S., and C. A. McCulloch. 2000. Partners in protection: interdependence of cytoskeleton and plasma membrane in adaptations to applied forces. *J. Membr. Biol.* 174:85–95.

Lee, H. S., S. J. Millward-Sadler, M. O. Wright, G. Nuki, and D. M. Salter. 2000. Integrin and mechanosensitive ion channel-dependent tyrosine phosphorylation of focal adhesion proteins and beta-catenin in human

articular chondrocytes after mechanical stimulation. *J. Bone Miner. Res.* 15:1501–1509.

Lehenkari, P. P., G. T. Charras, and M. A. Horton. 1999. New technologies in scanning probe microscopy for the understanding of molecular interactions in cells. *Expert Reviews in Molecular Medicine* at http://www-ermm.cbcu.cam.ac.uk.

Lehenkari, P. P., G. T. Charras, A. Nykänen, and M. A. Horton. 2000. Adapting atomic force microscopy for cell biology. *Ultramicroscopy.* 82:289–295.

Long, Q., X. Y. Xu, K. V. Ramnarine, and P. Hoskins. 2001. Numerical investigation of physiologically realistic pulsatile flow through arterial stenosis. *J. Biomech.* 34:1229–1242.

Malek, A. M., and S. Izumo. 1996. Mechanism of endothelial cell shape change and cytoskeletal remodeling in response to fluid shear stress. *J. Cell Sci.* 109:713–726.

Maniotis, A. J., C. S. Chen, and D. E. Ingber. 1997. Demonstration of mechanical connections between integrins, cytoskeletal filaments, and nucleoplasm that stabilize nuclear structure. *Proc. Natl. Acad. Sci. U.S.A.* 94:849–854.

Marotti, G., M. Ferretti, M. A. Muglia, C. Palumbo, and S. Palazzini. 1992. A quantitative evaluation of osteoblast-osteocyte relationships on growing endosteal surface of rabbit tibiae. *Bone.* 13:363–368.

McAllister, T. N., and J. A. Frangos. 1999. Steady and transient fluid shear stress stimulate NO release in osteoblasts through distinct biochemical pathways. *J. Bone Miner. Res.* 14:930–936.

Mente, P. L., and J. L. Lewis. 1989. Experimental method for the measurement of the elastic modulus of trabecular bone tissue. *J. Orthop. Res.* 7:456–461.

Nesbitt, S. A., and M. A. Horton. 1997. Trafficking of matrix collagens through bone-resorbing osteoclasts. *Science.* 276:266–269.

Niggel, J., W. Sigurdson, and F. Sachs. 2000. Mechanically induced calcium movements in astrocytes, bovine aortic endothelial cells and C6 glioma cells. *J. Membr. Biol.* 174:121–134.

Owan, I., D. B. Burr, C. H. Turner, J. Qiu, Y. Tu, J. E. Onyia, and R. L. Duncan. 1997. Mechanotransduction in bone: osteoblasts are more responsive to fluid forces than mechanical strain. *Am. J. Physiol. Cell Physiol.* 273:C810–C815.

Parkkinen, J. J., M. J. Lammi, R. Inkinen, M. Jortikka, M. Tammi, I. Virtanen, and H. J. Helminen. 1995. Influence of short-term hydrostatic pressure on organization of stress fibers in cultured chondrocytes. *J. Orthop. Res.* 13:495–502.

Peake, M. A., L. M. Cooling, J. L. Magnay, P. B. Thomas, and A. J. el Haj. 2000. Selected contribution: regulatory pathways involved in mechanical induction of c-fos gene expression in bone cells. *J. Appl. Physiol.* 89:2498–2507.

Picart, C., P. Dalhaimer, and D. E. Discher. 2000. Actin protofilament orientation in deformation of the erythrocyte membrane skeleton. *Biophys. J.* 79:2987–3000.

Radmacher, M. 1997. Measuring the elastic properties of biological samples with the AFM. *IEEE Eng. Med. Biol. Mag.* 16:47–57.

Rawlinson, S. C., A. A. Pitsillides, and L. E. Lanyon. 1996. Involvement of different ion channels in osteoblasts' and osteocytes' early responses to mechanical strain. *Bone.* 19:609–614.

Rawlinson, S. C., C. P. Wheeler-Jones, and L. E. Lanyon. 2000. Arachidonic acid for loading induced prostacyclin and prostaglandin E(2) release from osteoblasts and osteocytes is derived from the activities of different forms of phospholipase A(2). *Bone.* 27:241–247.

Reich, K. M., T. N. McAllister, S. Gudi, and J. A. Frangos. 1997. Activation of G proteins mediates flow-induced prostaglandin E2 production in osteoblasts. *Endocrinology.* 138:1014–1018.

Riemer-McReady, B., and S. J. Hollister. 1997. Strain concentrations surrounding an ellipsoid model of lacunae and osteocytes. *Computer Methods in Biomechanics and Biomedical Engineering.* 1:61–68.

Rosales, O. R., C. M. Isales, P. Q. Barrett, C. Brophy, and B. E. Sumpio. 1997. Exposure of endothelial cells to cyclic strain induces elevations of cytosolic Ca2+ concentration through mobilization of intracellular and extracellular pools. *Biochem. J.* 326(Pt 2):385–392.

Rubin, C. T., and L. E. Lanyon. 1984. Regulation of bone formation by applied dynamic loads. *J. Bone Joint Surg. [Am.].* 66:397–402.

Russell, B., D. Motlagh, and W. W. Ashley. 2000. Form follows function: how muscle shape is regulated by work. *J. Appl. Physiol.* 88:1127–1132.

Ryder, K. D., and R. L. Duncan. 2001. Parathyroid hormone enhances fluid shear-induced $[Ca^{2+}]_i$ signaling in osteoblastic cells through activation of mechanosensitive and voltage-sensitive Ca2+ channels. *J. Bone Miner. Res.* 16:240–248.

Sachs, F., and C. E. Morris. 1998. Mechanosensitive ion channels in nonspecialized cells. *Rev. Physiol. Biochem. Pharmacol.* 132:1–77.

Sakai, K., M. Mohtai, and Y. Iwamoto. 1998. Fluid shear stress increases transforming growth factor beta 1 expression in human osteoblast-like cells: modulation by cation channel blockades. *Calcif. Tissue Int.* 63: 515–520.

Salter, D. M., J. E. Robb, and M. O. Wright. 1997. Electrophysiological responses of human bone cells to mechanical stimulation: evidence for specific integrin function in mechanotransduction. *J. Bone Miner. Res.* 12:1133–1141.

Sato, M., K. Nagayama, N. Kataoka, M. Sasaki, and K. Hane. 2000. Local mechanical properties measured by atomic force microscopy for cultured bovine endothelial cells exposed to shear stress. *J. Biomech.* 33:127–135.

Schaffer, J. L., M. Rizen, G. J. L'Italien, A. Benbrahim, J. Megerman, L. C. Gerstenfeld, and M. L. Gray. 1994. Device for the application of a dynamic biaxially uniform and isotropic strain to a flexible cell culture membrane. *J. Orthop. Res.* 12:709–719.

Simon, B. R., M. V. Kaufmann, M. A. McAfee, and A. L. Baldwin. 1993. Finite element models for arterial wall mechanics. *J. Biomech. Eng.* 115:489–496.

Stamenovic, D., J. J. Fredberg, N. Wang, J. P. Butler, and D. E. Ingber. 1996. A microstructural approach to cytoskeletal mechanics based on tensegrity. *J. Theor. Biol.* 181:125–136.

Suchyna, T. M., J. H. Johnson, K. Hamer, J. F. Leykam, D. A. Gage, H. F. Clemo, C. M. Baumgarten, and F. Sachs. 2000. Identification of a peptide toxin from *Grammostola spatulata* spider venom that blocks cation-selective stretch-activated channels. *J. Gen. Physiol.* 115: 583–598.

Tagawa, H., N. Wang, T. Narishige, D. E. Ingber, M. R. Zile, and G. Cooper. 1997. Cytoskeletal mechanics in pressure-overload cardiac hypertrophy. *Circ. Res.* 80:281–289.

Timoshenko, S. P., and J. N. Goodier. 1970. Theory of Elasticity. McGraw-Hill, New York.

van Rietbergen, B., R. Muller, D. Ulrich, P. Ruegsegger, and R. Huiskes. 1999. Tissue stresses and strain in trabeculae of a canine proximal femur can be quantified from computer reconstructions. *J. Biomech.* 32: 443–451.

Wang, N., and D. E. Ingber. 1994. Control of cytoskeletal mechanics by extracellular matrix, cell shape, and mechanical tension. *Biophys. J.* 66:2181–2189.

Weinbaum, S., S. C. Cowin, and Y. Zeng. 1994. A model for the excitation of osteocytes by mechanical loading-induced bone fluid shear stresses. *J. Biomech.* 27:339–360.

Wozniak, M., A. Fausto, C. P. Carron, D. M. Meyer, and K. A. Hruska. 2000. Mechanically strained cells of the osteoblast lineage organize their extracellular matrix through unique sites of alphavbeta3-integrin expression. *J. Bone Miner. Res.* 15:1731–1745.

Wu, J. Z., and W. Herzog. 2000. Finite element simulation of location- and time-dependent mechanical behavior of chondrocytes in unconfined compression tests. *Ann. Biomed. Eng.* 28:318–330.

Wu, H. W., T. Kuhn, and V. T. Moy. 1998. Mechanical properties of L929 cells measured by atomic force microscopy: effects of anticytoskeletal drugs and membrane crosslinking. *Scanning.* 20:389–397.

Xia, S. L., and J. Ferrier. 1992. Propagation of a calcium pulse between osteoblastic cells. *Biochem. Biophys. Res. Commun.* 186:1212–1219.

Xu, Q. 2000. Biomechanical stress-induced signaling and gene expression

in the development of arteriosclerosis. *Trends Cardiovasc. Med.* 10: 35–41.

Yellowley, C. E., C. R. Jacobs, and H. J. Donahue. 1999. Mechanisms contributing to fluid-flow-induced Ca2+ mobilization in articular chondrocytes. *J. Cell Physiol.* 180:402–408.

You, J., G. C. Reilly, X. Zhen, C. E. Yellowley, Q. Chen, H. J. Donahue, and C. R. Jacobs. 2001. Osteopontin gene regulation by oscillatory fluid flow via intracellular calcium mobilization and activation of mitogen-activated protein kinase in MC3T3–E1 osteoblasts. *J. Biol. Chem.* 276: 13365–13371.

You, J., C. E. Yellowley, H. J. Donahue, Y. Zhang, Q. Chen, and C. R. Jacobs. 2000. Substrate deformation levels associated with routine physical activity are less stimulatory to bone cells relative to loading-induced oscillatory fluid flow. *J. Biomech. Eng.* 122:387–393.

Zaman, G., R. F. Suswillo, M. Z. Cheng, I. A. Tavares, and L. E. Lanyon. 1997. Early responses to dynamic strain change and prostaglandins in bone-derived cells in culture. *J. Bone Miner. Res.* 12:769–777.

Zhu, C., G. Bao, and N. Wang. 2000. Cell mechanics: mechanical response, cell adhesion, and molecular deformation. *Annu. Rev. Biomed. Eng.* 2:189–226.